Doctoral Thesis in Chemistry

Hierarchical adsorption at hair-mimetic interfaces

A neutron reflectivity study

SERENA COZZOLINO

KTH ROYAL INSTITUTE OF TECHNOLOGY

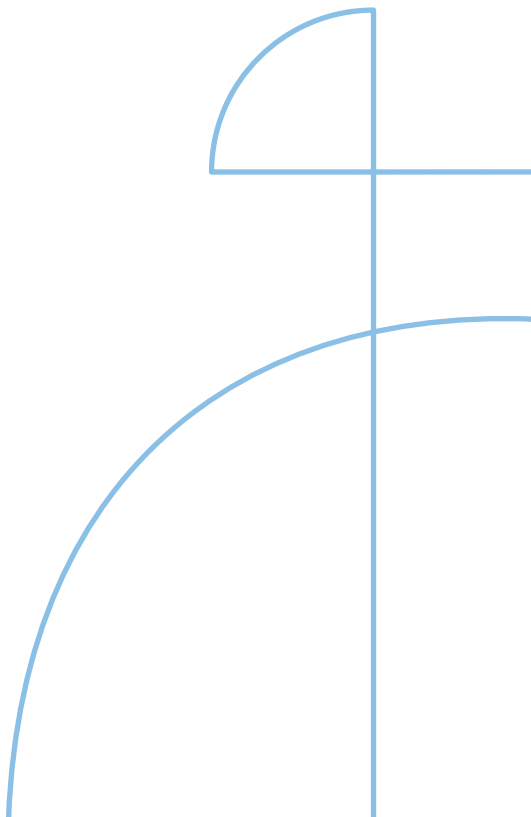

Hierarchical adsorption at hair-mimetic interfaces

A neutron reflectivity study

SERENA COZZOLINO

Academic Dissertation which, with due permission of the KTH Royal Institute of Technology, is submitted for public defence for the Degree of Doctor of Philosophy on Friday the 29th November 2024, at 2:00 p.m. in Kollegiesalen, Brinellvägen 6, Stockholm.

Doctoral Thesis in Chemistry
KTH Royal Institute of Technology
Stockholm, Sweden 2024

TRITA-CBH-FOU-2024:50
ISBN 978-91-8106-108-6

Printed by: Universitetsservice US-AB, Sweden 2024

“In primis, hominis est propria veri inquisitio atque investigatio”

Cicero, De Officiis

Serena Cozzolino, “Hierarchical adsorption at hair-mimetic interfaces: A neutron reflectivity study”, 2024, Department of Chemistry, School of Engineering Sciences in Chemistry, Biotechnology and Health, KTH Royal Institute of Technology, SE-100 44 Stockholm, Sweden

I. Abstract

Formulating a shampoo is a complex process that has to consider not only the diverse physicochemical properties of the hair fibre but also customers’ needs. For this reason, shampoos normally contain surfactants as cleansing base, polyelectrolytes for a conditioning effect and several additives. The existing products had years of optimization, but the current environmental issues require the cosmetic industry to switch to more sustainable formulations. To replace traditional ingredients with eco-friendly, bio-sourced ones, a detailed knowledge of the interactions happening at the hair surface is essential. This PhD project aimed at contributing to this knowledge by using neutron reflectometry (NR) to study the adsorption of model compounds to hair-mimetic surfaces. The advantage of NR over other surface techniques is its ability to characterize buried interfaces and define a hierarchy of adsorption from mixtures. The biomimetic models can be tuned to reproduce the hair surface in different conditions. A healthy fibre is hydrophobic, as it is covered by a layer of lipids, the main one being 18-methyleicosanoic acid (18-MEA), which has a characteristic methyl branch and is the subject of several studies due to its interesting properties. Due to weathering, ageing, or treatments like bleaching, the lipid layer can be damaged, and a hydrophilic surface is exposed. This modifies the interaction of the hair fibre with components of hair-care products. Complementing NR with other surface techniques, specific adsorption behaviours have been identified, addressing factors such as surface hydrophobicity, surfactant charge or polyelectrolyte size. Results indicate that, for example, the presence of the methyl branch of 18-MEA modifies the surface properties compared to a layer of straight chain lipids, or that a fully damaged hair model surface unexpectedly adsorbs a bilayer of anionic surfactant, thanks to the balancing of several factors playing a role in the interaction.

Keywords
Cosmetics, Neutron Reflectometry, Adsorption, Surfactants, Polyelectrolytes

II. Sammanfattning

Att formulera ett schampo är en komplex process som inte bara måste ta hänsyn till hårfiberns olika fysikalisk-kemiska egenskaper utan också till kundernas behov. Därför innehåller schampon normalt tensider som rengörande bas, polyelektrolyter för en vårdande effekt och flera tillsatser. De befintliga produkterna har optimerats under många år, men de aktuella miljöfrågorna kräver att kosmetikaindustrin byter till mer hållbara formuleringar. För att kunna ersätta traditionella med miljövänliga, biologiskt framställda ingredienser krävs detaljerad kunskap om de interaktioner som sker på hårets yta. Detta doktorandprojekt syftade till att bidra till denna kunskap genom att använda neutronreflektometri (NR) för att studera adsorptionen av modellföreningar till hårmimetiska ytor. Fördelen med NR jämfört med andra yttekniker är dess förmåga att karakterisera begravda gränssnitt och definiera en hierarki av adsorption från blandningar. De biomimetiska modellerna kan ställas in för att återge hårytan under olika förhållanden. En frisk fiber är hydrofob, eftersom den är täckt av ett lager lipider, varav den viktigaste är 18-metyleicosanoic acid (18-MEA), som har en karakteristisk metylgren och är föremål för flera studier på grund av sina intressanta egenskaper. På grund av vittring, åldrande eller behandlingar som blekning kan lipidlagret skadas och en hydrofil yta exponeras. Detta förändrar hårfiberns interaktion med komponenter i hårvårdsprodukter. Genom att komplettera NR med andra yttekniker har specifika adsorptionsbeteenden identifierats, med hänsyn till faktorer som ytans hydrofobicitet, ytaktiva ämnenas laddning eller polyelektrolyternas storlek. Resultaten visar t.ex. att närvaron av metylgrenen i 18-MEA förändrar ytegenskaperna jämfört med ett lager av rakkedjiga lipider, eller att en helt skadad hårmodellyta oväntat adsorberar ett tvåskikt av anjoniskt ytaktivt ämne, tack vare en balansering av flera faktorer som spelar en roll i interaktionen.

Nyckelord
Kosmetika, Neutronreflektometri, Adsorption, Tensider, Polyelektrolyter

III. Acknowledgments

I thought of moving this section at the end, but that's what anyone looks for, right? So I might just leave it here as the template suggests.

Everyone says that the PhD is more about the journey than the scientific results, and in these four years, living in two countries and three cities, many people and events had an impact on my journey.

To begin with, many thanks to Mark Rutland, Philipp Gutfreund, Alexei Vorobiev and Gustavo Luengo. Juggling four supervisors is not easy, but I'm really grateful that you chose me back then, giving me the opportunity to learn so much and grow professionally (and visit places, too!).

Mark, thanks for all the scientific and personal discussions; it was often challenging, but I appreciate you always tried to find the time. I will probably always do something you would advise me not to, but thanks for all your tentative coaching.

Philipp and Alexei, thanks for guiding me in the neutron universe, sharing your expertise and supporting me throughout the PhD. I am also thankful for all the other wonderful people I met in the LSS group, from the SuperADAM team to the soft matter folks (Olivier, Nico, Samantha, to cite just a few), and for those in the worldwide neutron community I had the chance to meet during beam times or conferences, in particular Andy Nelson, Deb Wakeham, Becky Welbourn. Among the ILL people, special thanks to Martina Sandroni for her patience in dealing with my not very nice chemicals and my random questions, I really appreciate all your help.

Gustavo and the people I met in L'Oréal, especially Andrew Greaves, Anne-Claude Dublanchet, Francesca Zuttion and the Imaging Unit, thanks for introducing me to the industrial world, my time there was short but eventful.

To my InnovaXN and ILL fellows, thanks for everything we shared – and here I take the opportunity to acknowledge the InnovaXN program, all this wouldn't have been possible without it.

Special mention to Wenke and Mohit, whom I met during my very first day at ILL, back in those crazy COVID times, and have been great friends ever since. To Yi Min, that approached me silently, like a cat, and like a cat just decided to

stay around (I know you will like this comparison). And to the big, (mainly) Italian group, starting from Ilaria and Isabella, that helped me at my lowest: Italians are a mess, we all know this… but luckily, they exist! I've had my (un)fair share of problems last year (that's where my pretentious opening quote stems from, in a Pindaric way), but I never felt alone thanks to you.

To the people in the Surface and corrosion science division at KTH, thanks for welcoming me last year, even if I arrived in an unfortunate moment. The special mention here goes to Marie and her cakes, you made my day more than once! Thanks to all the people roaming in Mark's group for sharing knowledge and experiences, in particular Sichao Li, who kindly helped me a lot in these past four years, remotely or in person, and Stuart Brown (a great teammate, despite his love for pineapple on pizza…).

I want to express my gratitude to the Scrittori Pigri ("lazy writers"), a group I casually bumped into and that means a lot to me now, with the formation of the Sciame Indolente (i.e., still lazy, but now we're bumblebees – it's a long story): you probably didn't realize that, but you rebuilt my self-confidence.

Thanks to my life-long friends Umberto and Eugenia, and to Federico, for being there through ups and downs.

Last but definitely not least, my heartfelt thanks to my family and to Alfredo: I know you would like me to be closer, but I also know you are ready to support all my choices, as long as I'm happy.

I'll stop it here, because if I were to list the names of all the people I'd like to thank (including some random Steve), that would probably take as many pages as my thesis. But if you are part of the groups I mentioned, or if we met in Grenoble or Stockholm in the past four years, you are likely on the list. I'm glad our paths crossed, and I'm looking forward to seeing you again, somewhere.

IV. List of publications

This thesis is based on the following publications:

I. Cozzolino S., Gutfreund P., Vorobiev A., Devishvili A., Greaves A., Nelson A., Yepuri N., Luengo G. S., Rutland M. W., "Mimicking the hair surface for Neutron Reflectometry", *Soft Matter*, 2024, 20, 7634-7645

II. Cozzolino S., Gutfreund P., Vorobiev A., Welbourn R. J., Greaves A., Zuttion F., Rutland M. W., Luengo G. S., "Adsorption hierarchy of surfactants and polymers to a damaged hair model: effect of composition, order and polymer size" *(under review)*

III. Cozzolino S., Gutfreund P., Odnevall I., Ibrahim R., Vorobiev A., Welbourn R. J., Zuttion F., Greaves A., Luengo G. S., Rutland M. W., "Adsorption of surfactants and polymers to biomimetic hair model surfaces" *(manuscript)*

IV. Cozzolino S., Gutfreund P., Nelson A., Recsei C., Vorobiev A., Greaves A., Luengo G. S., Rutland M. W., "Washing your hair with neutrons" *(manuscript)*

V. Contribution to the papers

I. Investigation; data analysis and visualization; writing – original draft

II. Investigation; data analysis and visualization; writing – original draft

III. Major part of investigation, data analysis and visualization; writing – original draft

IV. Part of conceptualization; investigation; data analysis and visualization; writing – original draft

VI. Additional publications

The following publication is not included in the thesis:

Batista M., Cozzolino S., Bergendal E., Vorobiev A., Fontaine P., Gutfreund P., Rutland M. W., "Nanodomains and the topography of water: An X-ray revelation of tuneable self-assembly in insoluble films" *(submitted)*

VII. List of abbreviations

18-MEA	18-methyl eicosanoic acid
18-MET	18-methyleicosane thiol
AFM	Atomic Force Microscopy
BT	1-butanethiol
cmc	Critical micellar concentration
CTAC	Cetyl trimethylammonium chloride
EA	Eicosanoic acid
ET	Eicosane thiol
GCMW	Gold contrast-matched water
GIXD	Grazing-incidence X-ray Diffraction
HDT	1-hexadecylthiol
MBT	2-methyl-1-butanethiol
NR	Neutron Reflectometry
ODT	1-octadecanethiol
pDADMAC	Poly(diallyl dimethylammonium chloride)
PS	Sodium 3-mercapto-1-propanesulphonate
QCM-D	Quartz-crystal microbalance with dissipation monitoring
SAM	Self-assembled monolayer
SDS	Sodium dodecyl sulphate
SLD	Scattering Length Density

SLES	Sodium lauryl ether sulphate
TTAB	Tetradecyl trimethylammonium bromide
XRR	X-ray Reflectometry

CONTENTS

1 Introduction

The current environmental issues call for actions to increase sustainability in every aspect of our society [1–3]. The cosmetic industry, with its continuously growing market [4], can surely have an impact on this, and, embracing the general trend, is committed to adopt more eco-friendly ingredients and processes [5,6]. To do this, a deeper scientific understanding of the system, i.e., of the cosmetic formulation and of its interactions with the consumer's skin or hair, is essential, in order to develop products with an improved environmental profile without losing their performance [5–7].

This thesis aims at contributing to this knowledge, specifically in the field of hair-care rinsing applications, by studying adsorption of selected compounds to hair-mimetic surfaces. The work is part of the doctoral program InnovaXN [8], a European project designed to bring together industries and large scale facilities, training students to bridge academic and industrial research and innovation challenges using the unique capabilities of neutron and synchrotron X-rays scattering techniques. The program covers a wide field of research areas and industrial sectors, with 10% of the projects targeting consumer products [8].

Such research can help working towards the Sustainable Development Goals (SDGs) defined by the United Nations (UN) (Figure 1.1) [9]. In the case of the cosmetic industry, the SDGs 3, 6, 7, 8, 9, 12, 13, 14 and 15 are relevant, as they address the use of resources, working conditions and climate change [10]. In particular, the use of bio-sourced or biodegradable ingredients in hair-care formulations is more respectful of life below water (SDG 14) and on land (SDG 15), besides relating to responsible consumption and production (SDG 12) and climate action (SDG 13) [10]. In fact, a major problem caused by current formulations is that at each stage of product production, use and disposal, substances of different toxicity may be dispersed in the environment [5,10]. The details can be assessed performing a life-cycle analysis, which gives information about the factors that affect sustainability, from raw materials to final disposal. While the cosmetic industry can adopt more eco-friendly processes to decrease

the environmental impact of its production stage, it cannot control at the same level the next steps in the product life cycle, which are influenced by the consumer. It can be foreseen, however, that rinsing of hair-care products leads to dispersion in the water stream of compounds, which can bio-accumulate and be toxic for aquatic life [5,10]. The choice of ingredients that are biodegradable (i.e., ecodesign of cosmetic products [11]) is then of utmost importance to align to the UN SDGs, but, as mentioned earlier, to keep meeting consumers' needs a deeper understanding of the properties of natural ingredients is required.

An example of bio-sourced alternative ingredient is chitosan, a polysaccharide which is a subject of extensive research due to its interesting properties and potential applications in different areas, including cosmetics [12,13]. One of the main focuses of this work was thus to investigate the adsorption properties of chitosan, in the absence and presence of selected surfactants, and compare it to synthetic polymers.

Figure 1.1 The 17 Sustainable Development Goals defined by the United Nations 9.

1.1 Aim of the project

This project is a collaboration involving KTH Royal Institute of Technology, Institut Laue-Langevin (ILL – Grenoble, France) and L'Oréal Research and Innovation (Aulnay-sous-Bois, France).

The aim is to gain a more detailed understanding of the interaction properties of hair, and how surfactants and polyelectrolytes adsorb depending on the specific structure of the hair surface.

To do this, hair-mimetic surfaces have been produced, so to separately address various features exposed by the hair fibre. The compounds that have been

selected for the adsorption studies are anionic (sodium dodecyl sulphate, SDS) and cationic (tetradecyl and hexadecyl trimethylammonium salts) surfactants, natural polysaccharides (chitosans of two different molecular weights) and a synthetic polymer (poly(diallyl dimethylammonium chloride), pDADMAC), in order to compare the effect of surfactant charge, the properties of natural and synthetic polyelectrolytes and how properties change when ingredients are mixed to mimic simplified shampoo formulations. An introduction to the structure of hair and cosmetic formulations is given in chapter 2, while a description of the hair-mimetic surfaces and the selected adsorbing species is in chapter 3.

The study was conducted mainly by Neutron Reflectometry (NR), as with this technique the structure of a layered system can be resolved, and the adsorption hierarchy can be defined based on the isotopic contrast of different molecules. For this reason, most of the work was carried out at the neutron facility ILL. NR experiments were complemented by quartz-crystal microbalance (QCM) measurements, to study the kinetics of the adsorption process. NR has a sub-nanometre resolution perpendicularly to the surface; however, it can only give averaged information in-plane. Therefore, Atomic Force Microscopy (AFM) was applied to probe the in-plane structure of the adsorbates; this was done during a secondment at L'Oréal. Chapter 2 contains a theoretical introduction to the three techniques mentioned here, while the experimental setup is illustrated in chapter 3.

2 Background

In this section, the structure of human hair and hair-care formulations are introduced, together with basic principles of the techniques used during the project.

2.1 The structure of hair

The fibre of human hair is composed of three main regions, that from centre to surface are the medulla, the cortex and the cuticle [14–16].

The organization of these structures has been thoroughly characterized by use of different techniques, such as small-angle X-ray scattering (SAXS) [17–20] or electron microscopy [21–24]. Figure 2.1 illustrates the substructures present in the hair fibre.

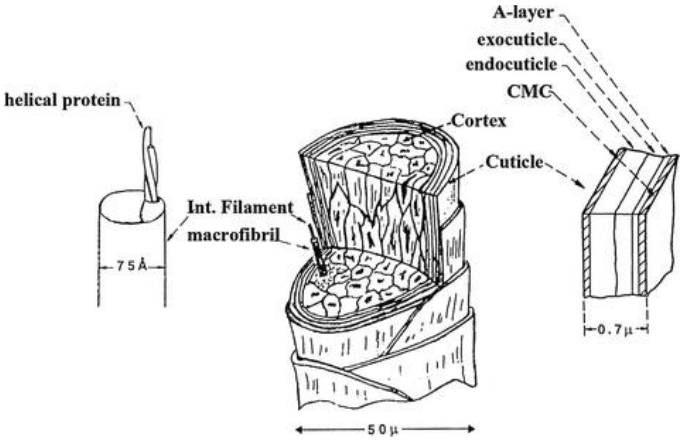

Figure 2.1 Stereogram of the hair fibre structure (CMC=Cell Membrane Complex). Reproduced from ref. 16 with permission from Springer Nature.

From a cosmetic perspective, the most interesting part is the external cuticle, as this is responsible for the interaction with hair-care formulations. The cuticle cells are organized in structures about 50 μm wide and partially overlapping like tiles, that form a thick protective layer for the inner cortex and medulla [19,25]. As shown in Figure 2.1, different layers can be distinguished in the cuticle, the outermost one being the A-layer, a cross-linked proteinaceous region with a high cysteine content [16].

The fibre is mainly composed by keratins [15,16,19], but lipids are associated with the keratinized structure and create a hydrophobic surface on the cuticle [18,26,27]. The lipid layer has a structural role; it increases the strength of the hair fibre [28] and reduces surface friction [28,29]. Hair lipids comprise fatty acids, triglycerides, cholesterol, squalene, wax esters and ceramides [18,28]. Fatty acids are mainly bound to keratins, via a thioester bond with cysteine residues [25,26,28,30], but the presence of free fatty acids has also been reported [18,31]. Among the bound fatty acids, the main component is the 18-methyleicosanoic acid (18-MEA) [26,27], which presents a characteristic antepenultimate methyl branch. This feature determines the specific properties of 18-MEA, such as the chain packing or the peculiar organization of an interfacial monolayer of free molecules [32,33]; moreover, a correlations has been reported between the absence of 18-MEA in the cuticle and the maple syrup urine disease [34].

From early studies, 18-MEA has been found to represent 41% of the lipid palisade on hair; the second most abundant component is the hexadecanoic acid (18%), but several other lipids are present (e.g., octadecanoic acid or eicosanoic acid), each at a concentration lower than 10% [26].

The specific composition of the lipid layer can be intrinsically different due to factors like ethnicity, gender or age [16,35,36], but it can also vary due to exposure of the hair fibre to external factors (weathering) or chemical treatments (e.g., bleaching). This causes an inhomogeneous distribution of lipids along the fibre, from root to tip [35,37], that can lead to fibre damage. A damaged hair surface shows a reduced content, or a total loss, of lipids, following the breakage of the thioester bond [25,38,39]. This translates to a dry and brittle fibre, with modified physico-chemical properties [28]. In fact, this process exposes the underlying proteins, and thus a hydrophilic surface. Moreover, the cysteine residues are oxidised to cysteic acid moieties, which confer an overall negative charge to the surface [25,29,38,39]. Specifically, it has been reported that sulphonate groups from the resulting cysteic acid tend to cluster, forming negatively charged patches on the hair fibre. The density of sulphonate moieties, averaged on the whole surface, is 2.2 molecules nm^{-2} [39].

2.2 Cosmetic formulations

A plethora of hair-care products exists to respond to different consumers' needs, from simple shampoos to deep conditioners and masks. The experiments presented in this thesis target shampoo ingredients, so this section will focus on such formulations.

Broadly, a shampoo contains three types of substances (even though the complete list of ingredients can have up to 30 entries) [7,25]. The main component of a shampoo is the cleansing base, i.e., the surfactant, present at a concentration of 10-20% by weight (w/w) [7,25]. The second type of ingredient is the conditioning agent, needed to counterbalance the surfactant tendency to dry out the hair fibre; cationic polyelectrolytes and silicones are used for this scope, at a percentage of 0.1-1% w/w [25,40]. The third group comprises various additives that can be needed to obtain the desired properties in the formulation (e.g., sodium chloride at a concentration of 100-500 mM to confer viscosity), agents with specific functionalities (e.g., anti-dandruff), perfumes… [7,25]

Surfactants are a class of compounds characterized by a polar headgroup and a hydrophobic tail. They are thus amphiphilic molecules with the ability to self-assemble, at concentrations above the critical micellar concentration (cmc), in structures depending firstly on their critical packing parameter (P_c), i.e., the ratio between the volume of the tail and its length and cross-sectional area of the headgroup [7,41,42]. The structures that surfactants can form depending on their P_c are illustrated in Figure 2.2.

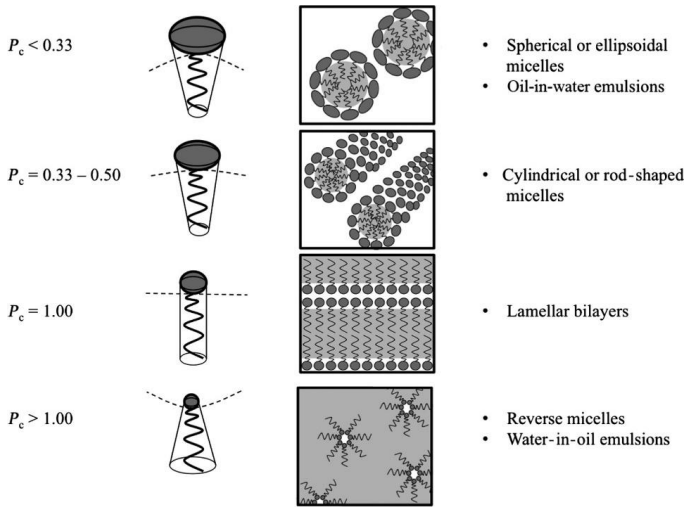

Figure 2.2 Schematic illustration of the structures formed by surfactants depending on their critical packing parameter P_c. Reproduced from ref. 7 with permission from John Wiley & Sons.

Surfactants used in shampoos normally have P_c <0.5, so they form micelles with a hydrophobic core that can solubilise sebum and various types of pollutants, while the hydrophilic shell keeps the aggregates soluble in water, executing in this way their cleansing activity. According to the charge of their headgroup, surfactants can be anionic, cationic, zwitterionic or non-ionic [42]. Shampoos contain mainly anionic species like alkyl sulphates or alkyl ether sulphates, the most common example being sodium lauryl ether sulphate (SLES) [7]. The choice of surfactant depends on a balance of different factors: their efficacy in removing sebum and soil, but also their mildness, foamability and cost. Alkyl and alkyl ether sulphates are effective, but they can irritate and sensitise the skin and dry hair, which has raised some concerns on their use [7]. The ethoxy groups (usually 1 to 5 units) in alkyl ether sulphates lowers the irritant effect, but they may contain trace amounts of 1,4-dioxane, which is a potential carcinogenic [43]. To reduce those drawbacks, other surfactants can be added (at a concentration of about 1% w/w), like cocamidopropyl betaine [7,41], which can also increase foamability. Also the fatty alcohols associated with sulphate surfactants [44], and resulting from their hydrolysis, are foam boosters [7] and able to decrease the surfactant cmc (it has been reported that higher cmc values correlate with higher toxicity of the surfactant [41]). Cationic surfactants are also used as secondary surfactants due to their conditioning properties and the formation, together with anionic surfactants, of lamellar structures with very low cmc [41]. In view of increasing the sustainability of hair-care products, a lot of research is conducted about biosurfactants, such as rhamnolipids [45], but a description of this class of compounds is beyond the scope of this thesis.

Moving to the second class of shampoo ingredients, the conditioning effect is mainly due to cationic polyelectrolytes. Having a positive charge, these compounds can interact with the negatively charged portions on the hair surface, forming a protective layer that restores the natural hydrophobicity of the surface. Polyelectrolytes, often polymers of quaternary ammonium species, associate with surfactants in the formulation and are deposited on the hair surface thanks to the formation of coacervates (liquid-liquid phase separation) during dilution in the rinsing process [7,40,46,47]. A category of very effective conditioning agents is formed by silicones, but concerns are raised relative to their environmental impact [41]. This prompted the research of biodegradable and bio-sourced alternatives such as the chitosan used in this thesis [5,13]. Chitosan is a polysaccharide, formed of D-glucosamine and N-acetyl-D-glucosamine units, that has several interesting properties. It is a deacetylated form of chitin, the main source of which is the shell of crustaceans. This poses the issue of possible allergic reactions; however, fungi can also produce chitosan, and this opens up the use of this compound in personal care products [12,13]. Chitosan has been reported to have anti-microbial, anti-oxidant and anti-inflammatory activity, and it is studied not only for its possible application in cosmetics but also as a carrier for drug delivery [12,13] or in skin tissue engineering [48–51] (besides other possible applications, e.g., food industry or water treatment [50]).

Compared to synthetic polymers, chitosan has a more rigid backbone and a lower charge density [12,52]. However, literature studies about chitosan/surfactant complexes indicate that aggregates with different characteristics can be obtained, and tuned adjusting factors such as pH, degree of deacetylation, nature of surfactant and ratio to chitosan [52].

2.3 Techniques to study adsorption

In this thesis, the adsorption to biomimetic surfaces is investigated. Several surface techniques are available for such studies, each presenting their own advantages and disadvantages. Some techniques were tested in the beginning of the project, i.e., ellipsometry and grazing-incidence X-ray diffraction (GIXD), but due to the choice of gold-coated substrates and the thin layer representing the biomimetic surface (both addressed in chapter 3), they could not be successfully employed (an example of GIXD is in chapter 4).

The main technique that was used during this project is Neutron Reflectometry (NR), that gives information about thickness and roughness of the adsorbed layers, and specifically can add details on the layer composition to define the hierarchy of adsorption from mixtures. NR experiments were complemented by quartz-crystal microbalance (QCM), which can describe the kinetics of the adsorption process as well as providing a measure of adsorbed mass, and by atomic force microscopy (AFM), that revealed the in-plane distribution of adsorbed species.

2.3.1 Neutron Reflectometry

Neutron reflectometry (NR) is a technique that allows the study of buried interfaces and the description of layered systems along the surface normal. It offers a unique insight for soft matter thanks to the peculiar distribution of neutron scattering properties along the periodic table.

The scattering interaction between matter and probe (neutron or X-rays) can be described by a parameter called scattering length, which is correlated to the differential scattering cross-section of a sample [53]. Multiplying the scattering length (b) of an element by its isotope number density (N), a quantity called scattering length density (SLD) is determined. For X-rays, the SLD varies proportionally to the atomic number, is always positive and can have a non-negligible imaginary component due to the possibility of adsorption [53]. For neutrons, the SLD varies in a more complex manner, with no specific trend along the periodic table. In particular, the interaction of neutrons with hydrogen is completely different to that with deuterium. The SLD value is $-1.58*10^{-6}$ Å^{-2} for hydrogen and $2.82*10^{-6}$ Å^{-2} for deuterium [54], the interaction with the former being attractive and the latter repulsive. This creates the possibility of scattering contrast by isotopic variation, which in turn allows the description of the

hierarchy of adsorption if the components of the mixture have different isotopic contrast (that is why a choice was made of using deuterated surfactants and hydrogenous polyelectrolytes).

In NR, the signal comes from the (specularly) reflected neutron beam at the various interfaces in the sample. In fact, when a neutron beam is shined on a surface at low incidence angles, it is partially reflected and partially refracted to the next layer. Figure 2.3 illustrates the process.

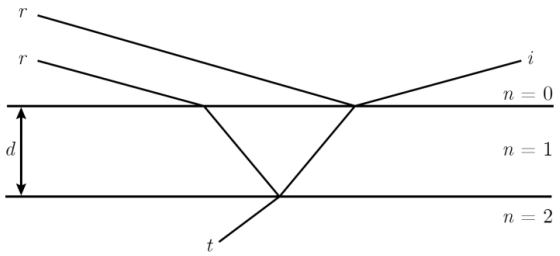

Figure 2.3 Schematic drawing of a neutron beam (i) impinging on a surface and being transmitted (t) and reflected (r) at the interfaces of a layer of thickness d. Reproduced from ref. 55 (CC BY-SA 4.0 license).

The difference between the wavevectors associated to incident (or initial, $\overrightarrow{k_i}$) and reflected (or final, $\overrightarrow{k_f}$) beam is the momentum transfer Q, whose vector (in the considered specular geometry) is perpendicular to the surface, so it is influenced by the sample structure along the surface normal; it depends on the angle of incidence θ and on the neutron wavelength λ [56]:

$$Q = \left|\overrightarrow{k_f} - \overrightarrow{k_i}\right| = \frac{4\pi}{\lambda}\sin\theta$$

Thus, scanning a range of neutron wavelengths or incidence angles, having at each point a sum of the neutron beams reflected at the various interfaces of the system, a curve is obtained, characterized by a first region of total reflection (reflectivity R = 1), followed by a modulated exponential decay.

The Q value up to which R = 1 depends on the sample composition. In fact, the scattering interaction can be treated according to classical optics, defining a refractive index for neutrons as a function of the SLD. From this, a critical angle of total external reflection (θ_c) is determined [56]:

$$\theta_c \sim \lambda\sqrt{\frac{Nb}{\pi}}$$

Substituting this in the previous definition of Q, the corresponding critical momentum transfer Q_c is obtained (the equation is valid for a single interface; for multiple interfaces the difference in SLD across the sample determines Q_c). At larger Q, the signal decays proportionally to Q^{-4}, and if more than one interface is present in the sample, this decay is modulated by a combination of the signals coming from the layers. This gives rise to the so-called Kiessig fringes [56,57], the spacing and amplitude of which depends on the thickness, roughness and composition of the sample. An example of a reflectivity curve is shown in Figure 2.4.

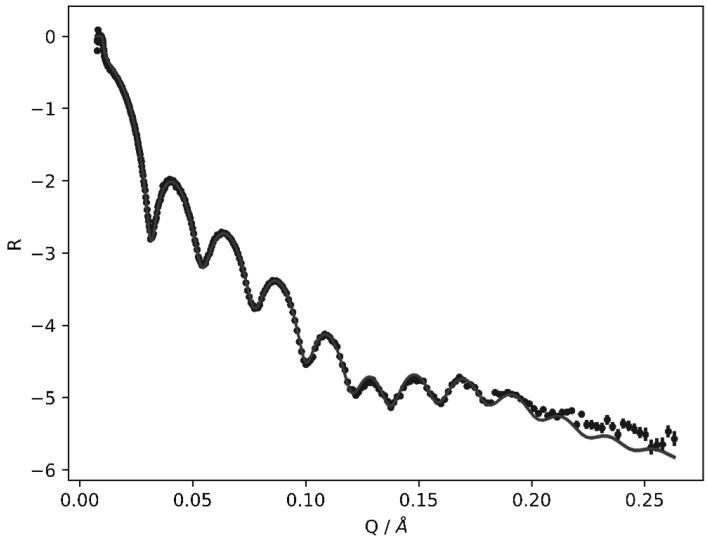

Figure 2.4 Example of reflectivity curve, obtained for a gold-coated silicon block used in this thesis. $Q_c \sim 0.01$ Å^{-1}. The dots are the experimental datapoints, the solid line is the fitted curve (more details on the fitting method are in section 3.2.1).

The analytical description of such curves is based on recursive methods such as those developed by Parrat [58] or Abelès [59] starting from the Fresnel equation for the reflectivity at a single interface. A complete description of these approaches can be found in the literature [60–64]. Fitting models based on the recursive methods return a SLD profile, that displays a description of the sample: the compositional information can be extracted from the SLD value on the y-axis, the thickness of the various layers from the x-axis, and the roughness or interdiffusion across an interface can be seen in the sharpness of the step between two layers in the SLD profile. Figure 2.5 shows the SLD profile corresponding to the NR curve in Figure 2.4.

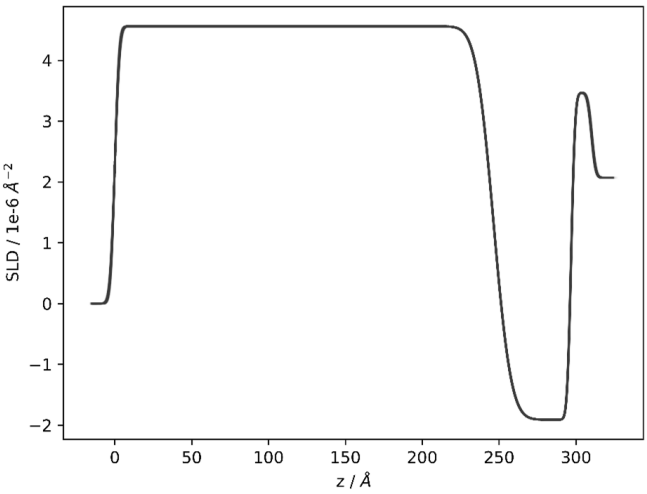

Figure 2.5 SLD profile corresponding to the NR curve in Figure 2.4. Layers from right to left are Si, SiO_2, Ti, Au, air.

The SLD profile above is composed of the following materials, whose SLD is indicated in parenthesis: silicon ($2.07*10^{-6}$ Å^{-2}), silicon dioxide ($3.47*10^{-6}$ Å^{-2}), titanium ($-1.91*10^{-6}$ Å^{-2}) and gold ($4.56*10^{-6}$ Å^{-2}). The interfaces are sharp, less so only at the Au/Ti interface. Roughness or interdiffusion, however, cannot be distinguished by NR as the information that is obtained is averaged in-plane, over the coherence volume of the neutron beam [56,65], but the effect of dampening the reflectivity can be described in a way similar to the Debye-Waller factor, that accounts for the decrease in diffracted intensity [56,65].

As mentioned in the beginning, a reflectivity curve can be obtained either by scanning a range of incidence angles or neutron wavelengths.

In the first case, one neutron wavelength is selected thanks to a monochromator, and angles up to ~5° are explored. The drawback of this approach is the higher sensitivity to sample over-illumination. In fact, at very small angles of incidence, the footprint of the neutron beam is normally larger than the sample area. As θ increases, however, this effect gradually diminishes. More information on over-illumination is given in section 3.2.1.

The second case is used in Time-of-Flight (ToF) instruments, where multiple neutron wavelengths are collected simultaneously at a fixed incidence angle (normally two angles are selected to cover a broader Q range). Neutrons are distinguished and detected based on the time it takes to travel between two choppers, as their velocity is correlated to their wavelength. With this setup, a

constant area is illuminated, and it can be selected by properly setting the aperture of slits along the beam path, to avoid over-illumination.

2.3.2 Quartz-crystal Microbalance

As the name suggests, the quartz-crystal microbalance (QCM) is based on the use of a quartz crystal sensor, to study the adsorption process in a wide range of cases. The sensor has a specific resonance frequency, according to which it oscillates when a voltage is applied to the electrodes on the crystal. If molecules adsorb on top of the crystal, its resonance frequency changes, proportionally to the adsorbed mass. In the simplest case, the frequency shift Δf can be related to the adsorbed mass Δm by the Sauerbrey equation $\Delta m = -C * \Delta f / n$, where C is a constant that depends on the crystal and n is the overtone number [66].

A QCM instrument monitors the frequency shift for the fundamental frequency plus its overtones from n=3 to n=13. Overtones have different penetration depth $\delta = \sqrt{2\eta / \omega\rho}$ (η is the viscosity of the medium, ω the angular frequency and ρ the density), meaning they can probe different distances from the surface. In addition to that, current instruments also record the energy dissipated during the adsorption process, i.e., the ratio between the stored and the lost energy when oscillating (QCM-D, quartz-crystal microbalance with dissipation monitoring). This adds information on the viscoelastic properties of the adsorbed layer, which can also influence the frequency shift. In this case, the Sauerbrey equation fails, and more complex models are needed to analyse the QCM-D signal [67]. These models are based on the description of viscoelastic behaviour by Maxwell and Voigt [68]. In particular the Voigt (or Kelvin-Voigt) model has been developed as it is more relevant for the timescale of a QCM experiment [67,68], although some polymers and surfactants have been reported to behave like Maxwell fluids [68,69].

An example of QCM-D measurement is in Figure 2.6. The figure shows the adsorption of chitosan on a hair-mimetic surface (partially damaged hair model, paper II). When chitosan is injected in the cell, there is a clear decrease in the frequency value, indicating that additional mass is bound to the crystal. There is a small spreading of the overtones, both for the frequency and the dissipation shift, indicating a change in viscoelasticity on the surface. It is known that chitosan, as other polyelectrolytes, does not adsorb, in fact, as a homogeneous rigid layer [70,71]. After rinsing, there is no variation in the signal, suggesting an irreversible adsorption. This data is further discussed in paper II.

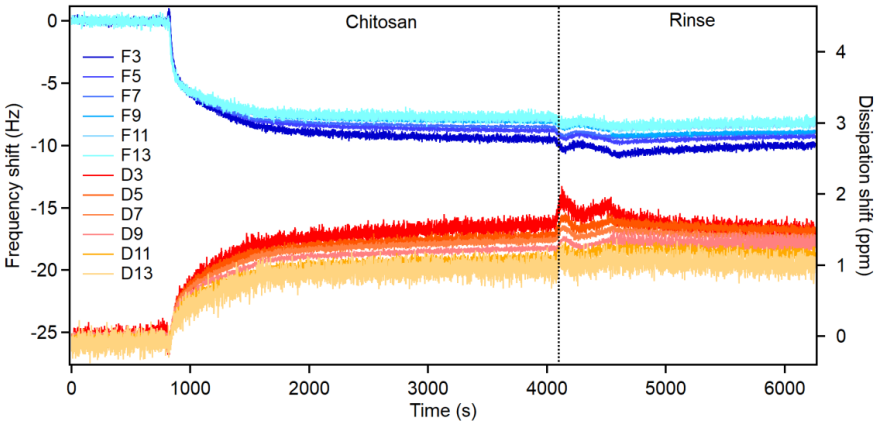

Figure 2.6 QCM-D measurement - adsorption of chitosan on a hair-mimetic surface.

2.3.3 Atomic Force Microscopy

Atomic force microscopy (AFM) is based on the use of a cantilever with piezoelectric components that is deflected by the interaction with the sample, depending on the height of the surface features and the force between surface and tip [72]. A simplified description of the instrument components is in Figure 2.7.

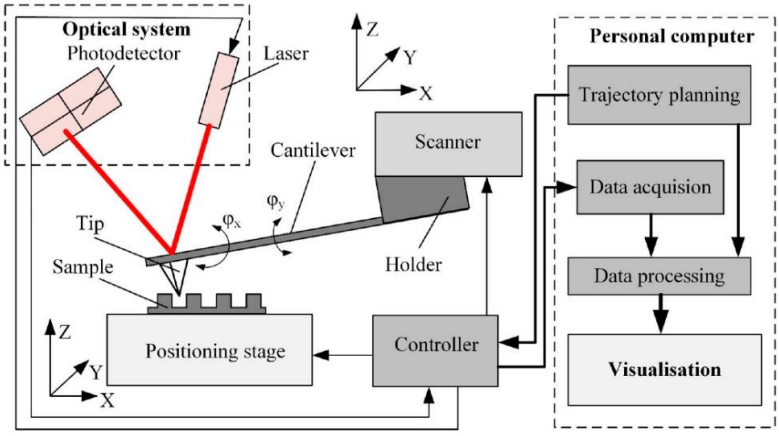

Figure 2.7 Schematic illustration of the AFM system. Reproduced from ref. 73 (CC-BY 4.0 license)

The deflection is monitored by a feedback loop: a laser is shined on the back of the cantilever and reflected on a position-sensitive photodiode. A deflection of the cantilever will modify the position of the laser beam on the photodiode, and while scanning the surface these shifts can be used to map the sample. There are various modes of operation of an atomic force microscope [74]. For this project, the dynamic, or "tapping", mode [74] has been chosen: in this mode, the tip is oscillated near the surface and the feedback system monitors the amplitude of the oscillation and maintains it constant during sample scanning. This is preferred to the contact mode when imaging soft samples because of the lower damage or deformation to the surface and the higher resolution thus achieved [74,75]. In addition to the surface topography, it is possible to obtain information on adhesion and mechanical properties of the sample by operating the instrument in PeakForce Quantitative Nanomechanics (QNM) mode [76]. In this way, force curves are obtained from which the Young's modulus can be derived [77]. To obtain a force curve, an example of which is presented in section 3.4, the tip approaches the sample until the sensed force (calculated from the tip deflection d and the cantilever spring constant k according to Hook's law: $F = -kd$) reaches a preset value, then it retracts. The approach trace gives information on the elastic properties of the sample, while the retract part depends on inter- and intramolecular interactions in the sample [77].

3 Materials and methods

Organosulphur compounds, and especially alkyl thiols, have been extensively used to produce self-assembled monolayers (SAMs) on gold, as such functionalised surfaces are versatile and easy to prepare [78,79]. Thiol SAMs have then been chosen to mimic various features of the hair fibre, an approach which has already few examples in the literature [80–83]. In this chapter, the preparation of hair-mimetic surfaces is described, as well as the experimental procedure for the adsorption studies, while the theory behind was summarized in chapter 2.

3.1 Thiol surfaces and chemicals

SAMs can be obtained by immersing a gold-coated substrate in a dilute thiol solution. Several studies have attempted to optimize parameters such as solvent, temperature, thiol concentration and incubation time to obtain high-quality SAMs [78,79,84]. The conditions applied here are based on common literature procedures. Gold-coated substrates were incubated in 1 mM solutions of the selected thiol in absolute ethanol (in the case of mixtures of two thiols, the total concentration was 1 mM) for at least 15 h (overnight incubation), but up to 24 h for some systems, as described later in this section.

The thiols have been chosen to either represent the hydrophobic surface of a healthy fibre, or the hydrophilic and negatively charged surface of a damaged fibre (see section 2.1 for a description of the structure of hair). In each case, SAMs produced by commercially available, short-chain (hydrogenous) thiols have been studied first, then the models have been improved with custom-made, long-chain thiols. Names and structures (drawn using ChemDraw [85]) of the selected molecules are presented below.

Healthy hair models:

- 2-methy-1-butanethiol (MBT): it has an antepenultimate methyl branch that mimics the one present in the most abundant hair lipid, i.e., 18-MEA [26].
- 1-butanethiol (BT): the straight-chain analogue, to investigate the effect of the methyl branch on the interaction properties of hair. BT and MBT were purchased from Sigma-Aldrich.

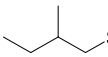

2-methyl-1-butanethiol (MBT)

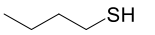

1-butanethiol (BT)

- N-(2-sulfanylethyl)18-methyleicosanamide, as thiol derivative of 18-MEA, referred to, in this thesis, as 18-MEA thiol. It is designed to maintain the carbonyl moiety of the hair lipid.

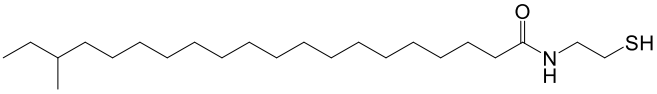

N-(2-sulfanylethyl)18-methyleicosanamide (18-MEA thiol)

- N-(2-sulfanylethyl)eicosanamide (referred to as EA thiol), the thiol derivative of the straight chain analogue eicosanoic acid (EA). 18-MEA thiol and EA thiol were provided by L'Oréal.

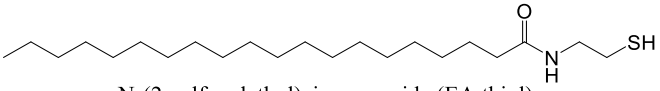

N-(2-sulfanylethyl)eicosanamide (EA thiol)

- Deuterated d-43 18-methyl-1-eicosanethiol (d43-18-MET): deuterated thiol derivative of 18-MEA. To make the synthesis of the deuterated chemical more feasible, it has been preferred, in this case, to reduce the carboxylic group of 18-MEA obtaining a simple alkyl thiol.

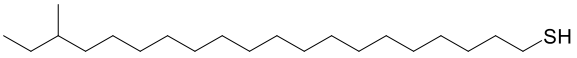

18-methyl-1-eicosanethiol (18-MET)

- Deuterated d-41 1-eicosanethiol (d41-ET): deuterated thiol derivative of EA, in which the carboxylic group was reduced, as for d43-18-MET. d-18-MET and d-ET were produced by the National Deuteration Facility at ANSTO (Australian Nuclear Science and Technology Organisation) [86].

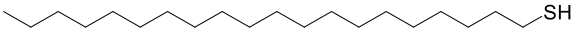

1-eicosanethiol (ET)

- 1-hexadecanethiol (HDT): thiol derivative of the second most abundant hair lipid, hexadecanoic acid [26], in which the carboxylic group is reduced. HDT was purchased from Sigma-Aldrich.

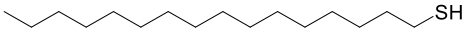

1-hexadecanethiol (HDT)

- 70:30 d-18-MET:HDT: this mixture reproduces the ratio of the two most abundant hair lipids [26], so it is the best model to represent the layer structure and chain packing in the lipid palisade.

Damaged hair models:

- Sodium 3-mercapto-1-propanesulphonate (PS): the terminal sulphonate group mimics the moiety that is exposed, upon removal of lipids, from the underlying proteins (section 2.1), so it reproduces a fully damaged hair surface. PS was purchased from Sigma-Aldrich.

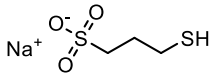

sodium 3-mercapto-1-propanesulphonate (PS)

- 50:50 MBT:PS: this model represents the intermediate characteristics, in terms of surface charge and hydrophobicity, of a partly damaged hair surface.
- 20:80 18-MEA thiol:PS: compared to the previous model, this one adds the mismatch in chain length that better mimics the features of a partly damaged hair fibre.

The ratios indicated for the mixtures of thiols are those of the species in solution, which do not necessarily correspond to the ratio of adsorbed thiols on the surface [78] (the resulting surface ratios will be discussed in chapter 4). Substrates to be functionalized with mixtures of thiols were immersed overnight as different thiols can adsorb with different affinities, and increasing the incubation time may lead in the extreme case to full replacement on the surface by the preferred adsorbing species. MBT and BT surfaces were also prepared by overnight incubation, while for the other thiols the time was increased to 24 h. In fact, despite adsorbing already within a few minutes, it has been observed that the forming monolayer can rearrange for days (even though average properties do not significantly change anymore after about 12-18 h) [78], thus a longer incubation time was preferred for the long-chain thiols. Regarding pure PS, the incubation time was also 24 h, because it has been reported that the SAM formed by PS has a low coverage [87], so a longer time was chosen to minimize defects in the monolayer. After functionalization, the surfaces were rinsed with absolute ethanol to remove the excess physisorbed thiol, dried with nitrogen and either immediately used for experiments or, if needed, stored under inert gas (argon or nitrogen).

The species selected for the adsorption studies, mentioned in section 1.1, are listed below, and structures are in Figure 3.1.

Surfactants:

- Sodium dodecyl sulphate (SDS), either hydrogenous (h-) or deuterated (d25-, both purchased from Sigma-Aldrich) as an example of a widely used anionic surfactant.
- Tetradecyl trimethylammonium bromide (TTAB) and hexadecyl (also named cetyl) trimethylammonium chloride (CTAC), both deuterated (d38- and d42-, CDN Isotopes), as examples of cationic surfactants, to study the effect of headgroup charge on adsorption.

Polyelectrolytes:

- Chitosan, of fungal origin, provided by L'Oréal in two forms: a 3 kDa molecule (degree of deacetylation >97%), which is referred to as oligomer, and a 27 kDa one (degree of deacetylation >95%), referred to as polymer. They were chosen as sustainable alternatives to synthetic polymers.
- Poly(diallyl dimethylammonium chloride) (pDADMAC, Sigma-Aldrich), as an example of synthetic polymer commonly found in cosmetic formulations.

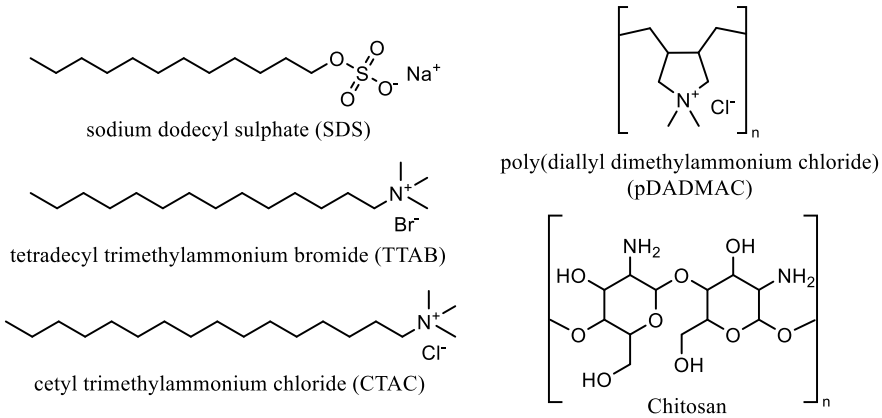

Figure 3.1 Structures of selected surfactants (left) and polyelectrolytes (right).

Solutions were freshly prepared just before an experiment. The appropriate amount of each compound was weighed and dissolved in either water (Milli-Q quality, Millipore), or, for the neutron experiments, in a mixture of Milli-Q and deuterated (Sigma-Aldrich) water (see section 3.2 for more details). In both cases, the solvent contained sodium chloride (at a concentration of 100 mM NaCl) to maintain a constant ionic strength. The pH was routinely measured and normally found to be ~ 6. Only in the case of chitosan polymer was the pH 4 as this species requires acetic acid to dissolve. The oligomeric form, instead, is soluble in water even at neutral pH.

The polyelectrolytes were used at a concentration of 100 ppm, while the concentration of surfactants was defined in terms of multiples of the critical micellar concentration: 8 mM or 1.5 mM for SDS in the absence or presence of 100 mM NaCl, respectively [88]; 0.065 mM for CTAC in 100 mM NaCl [89]; 0.87 mM for TTAB in 100 mM NaCl [90].

3.2 Neutron Reflectometry

Neutron reflectometry (NR) was the main technique used to study adsorption to the hair-mimetic surfaces, since the high sensitivity for the hydrogen/deuterium contrast allows investigating the hierarchy of adsorption from mixtures of surfactants and polyelectrolytes, an aspect which cannot be unravelled by other surface techniques. A theoretical description of NR is in section 2.3.

The NR experiments were performed at different facilities, on the neutron reflectometers listed in **Table 3.1**. The first three instruments in the table are located at ILL, while INTER is located at the ISIS Neutron and Muon Source (UK) and Platypus at the Australian Centre for Neutron Scattering (ACNS, Australia).

Table 3.1 Instruments used for the performed NR experiments.

For each reflectometer are listed the type, i.e., whether it is monochromatic or time-of-flight (ToF), with the corresponding wavelength or angle setup; the scattering geometry; the papers where the experiments are described.

Instrument	Type	Scattering plane	Related papers
SuperADAM [91]	Monochromatic (λ = 5.21 Å)	Horizontal	I, III
FIGARO [92]	ToF (θ_1=0.8°, θ_2=3.2°)	Vertical	III
D17 [93]	ToF (θ_1=0.8°, θ_2=3.2°)	Horizontal	II
INTER [94]	ToF (θ_1=0.7°, θ_2=2.3°)	Vertical	II, III
Platypus [95]	ToF (θ_1=0.65°, θ_2=3°)	Vertical	I, IV

For the various experiments, gold-coated silicon blocks were employed, but the characteristics were different depending on the coating provider. The deposition process requires first the deposition of an adhesion layer, which can then be coated by gold. Most of the blocks had an adhesion layer of a few nm of titanium, but some presented a ~12 nm layer of chromium instead. In both cases, they

were subsequently coated by a layer of about 20 nm of gold, with roughness ≤ 1 nm. The presence of the chromium layer was found to be not optimal for such experiments, as will be explained in section 3.2.1.

When possible, the bare gold-coated blocks were characterized in air by NR prior to functionalization. However, due to time constraints and beam time availability, in some cases the characterization of the substrates was done by XRR, using an Empyrean X-ray platform (Malvern Panalytical) equipped with a copper source.

After functionalization, the thiolated blocks were mounted, depending on their size, in one of the solid/liquid cells illustrated in Figure 3.2.

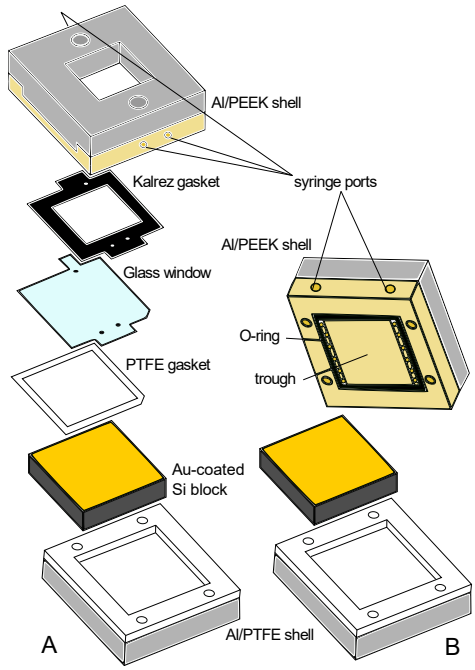

Figure 3.2 Expanded view of the solid/liquid cells used in the NR experiments. A) "custom" 65*65 mm^2 cell, similar to the one used by Pilkington *et al.* [96]. The liquid phase is injected through the ports in the PEEK shell and contained in the trough formed by the PTFE gasket between the gold surface and the glass window; B) "typical" 50*50 mm^2 cell, where the trough is in the PEEK shell, sealed by an O-ring. Reproduced from paper I (CC-BY 3.0 license).

For some experiments, blocks with a surface of 80*50 mm^2 were used, which could be mounted in a rectangular cell whose structure is similar to that in Figure

3.2 B. It is worth noting that the scattering geometry for air/solid and solid/liquid measurements is reversed, i.e., in the first case the neutron beam is shined through air on the gold surface and transmitted across the block to silicon, while in the second case the neutron beam crosses the silicon layer first and is transmitted in the opposite direction. This is because of the incoherent scattering of the liquid that would attenuate the neutron beam, while for silicon the attenuation is low [63,64,97].

For all the experiments, the temperature was maintained constant by connection to a water bath set at 22 °C. Most of the experiments were conducted using as solvent a 74:26 D_2O:H_2O mixture, i.e., gold contrast-matched water (GCMW) as its SLD is similar to gold ($4.6 * 10^{-6}$ $Å^{-2}$). This offers a good scattering contrast to both the thiol and the adsorbed species. To enhance the contrast and obtain information on the hierarchy of adsorption and distribution of species perpendicularly to the surface, it was chosen to use hydrogenous polyelectrolytes and (mostly) deuterated surfactants (since they are easier to obtain and commercially available). In some cases, hydrogenous surfactants were also used, see e.g., paper IV. (However, the use of pure D_2O or H_2O would mask the contribution of components of like isotopic contrast, so a mixture of intermediate SLD was preferred.)

The exact adsorption sequences can be found in the *Materials and methods* section of each paper. They were designed to study the following effects:

- Absence of salt (one test measurement on the MBT surface, showed in paper I)
- Increasing concentrations of surfactant, and comparison between anionic and cationic ones: the selected concentrations correspond to 0.1, 0.5, 2 and 20 cmc, with the exception of TTAB (paper IV), which was used at a concentration of 6 cmc to simulate the correct anionic to cationic surfactant ratio in the presence of 20 cmc SDS
- The order of injection of surfactant and polyelectrolyte (e.g., how adsorption of a solution of SDS changes before and after exposure of a partially damaged hair model to chitosan – paper II)
- Hierarchy of adsorption from mixtures of surfactant and chitosan oligomer or from a mixture of two surfactants: cosmetically relevant ratios for the mixtures were calculated based on the highest SDS concentration applied, i.e., 20 cmc. As introduced in section 2.2, shampoo formulations contain 10-20% w/w anionic surfactant. 20 cmc being about 1% w/w, the used concentrations of the other component were scaled accordingly (e.g., as polyelectrolytes are present at levels of 0.1-1% w/w, chitosan was introduced at a concentration of 100 ppm = 0.01% w/w)
- Synthetic vs natural polymers, and different molecular weights of the latter (paper II and III)

The reduction of NR data was performed with different software depending on the instrument on which they were collected: pySAred [98] for SuperADAM data, COSMOS [99] for FIGARO and D17 data, Mantid workbench [100] for INTER data, and a Jupyter notebook for Platypus data. In general, data reduction involves integrating the 2D reflectivity maps and converting the angle or wavelength axis to obtain a reflectivity curve as a function of the Q vector. In addition to this, with pySAred the region of total reflection is corrected by accounting for over-illumination of the sample, then the curves are scaled to have a reflected intensity of 1 at very low Q values, and, if needed, corrected for alignment offsets. The reduction tools for the ToF reflectometers, instead, apply a normalization of the data to the direct beam, data binning in the desired timeframe and, except for Mantid, background subtraction.

3.2.1 NR data fitting and method development for the over-illumination issue

Reduced data were fitted using RefNX [101]. The fitting procedure was based on a standard slab model (a microslicing method [102], although more versatile and in principle suitable to interpret complex adsorption profiles, resulted in the appearance of artefacts in the SLD profile and could not be implemented successfully). With the slab model, the layers that compose the sample are each described by a slab of defined thickness, roughness (described by an error function [56]) and SLD. Those parameters were fitted by a differential evolution algorithm [103], which, from the initial guess, varies each parameter in the defined ranges by application of so-called mutation and selection steps; the obtained values are compared to the experimental data and the process is repeated until convergence. As this method can lead to a local minimum, the validity of the fitted curve was checked by Markov-Chain Monte Carlo (MCMC) analysis [55,101]. The MCMC analysis explores the whole fitting range with random guesses and returns a covariance matrix in the form of a corner plot. It basically summarises whether the solution obtained by differential evolution is unique or not. The settings for the MCMC analysis need to be chosen to sample appropriately the range of fitting parameters. For the presented data, sampling was run for 5000 steps, then the obtained chains were processed applying a burn-in phase of 400 steps and thinned by 400 as well, to reduce autocorrelation.

The slab model of the gold-coated silicon substrate was fitted on the reflectometry data (either NR or XRR) of the bare block. An example of the covariance matrix obtained from an MCMC analysis is shown in Figure 3.3 (fitted NR data of a clean gold-coated silicon block with chromium adhesion layer). The squares along the matrix diagonal indicate the distribution of each fitted parameter in the given range, while off diagonal squares represent the correlation between the parameters along rows and columns. A strong correlation is inferred from a diagonal (instead of a circular) distribution, like for the third row/third column (counting from the bottom left corner)

intersection: the two parameters are the thickness of silicon dioxide and of the adhesion layer, which can often be interdiffused or very rough, making a clear distinction of the interface difficult. The two bottom rows refer to the roughness of the furthest interfaces from the incident neutron beam (in this case, Si/SiO_2 and SiO_2/Cr). It has been observed that often these parameters have little influence on the NR curve, so they might result equally distributed across the whole chosen range (see an example in the ESI of paper I, Figure S14) or tend to the limit values as in this example.

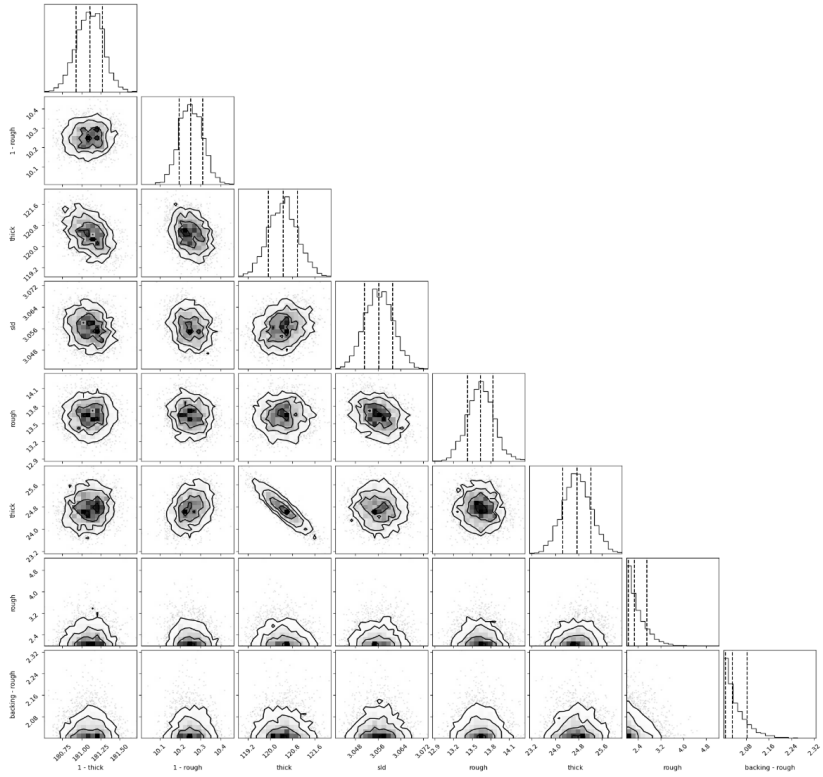

Figure 3.3 Corner plot obtained by MCMC analysis of the NR data for a gold-coated silicon block in air. Slabs: air/Au/Cr/SiO_2/Si.

The results were used for the subsequent fitting of the solid/liquid data. To describe the thiol layer, one slab was added to the model of the substrate and its parameters fitted. Then, for the successive adsorption steps, the thiol layer was considered unperturbed and one more slab was added to define the adsorbed layer (an exception needed to be done for some long-chain thiol surfaces, as explained in section 4.2). If the fit did not look satisfactory by eye, a second slab was added. However, no prior assumption was made on the nature of the

adsorbed layer, so in the case of mixtures, the whole range of SLD values defined by the pure (dry) substances was explored. The reference values of the dry molecules, obtained from the NIST calculator [54], are listed in **Table 3.2**. In the case of chitosan, the reported SLD value considers that chitosan has four exchangeable protons, and that in GCMW the H/D ratio is ~1/3.

Table 3.2 Density and SLD values of the species employed for NR experiments

Thiols	Density (g cm^{-3})	SLD (*10^{-6} Å^{-2})	*Surfactants*	Density (g cm^{-3})	SLD (*10^{-6} Å^{-2})
MBT	0.85	-0.25	h-SDS	1	0.28
BT	0.84	-0.24	d25-SDS	1.1	6.2
PS	1.4	1.1	d25-dodecanol	0.8	6.1
18-MEA thiol	0.85	-0.015	d38-TTAB	1	6.15
EA thiol	0.85	-0.004	d42-CTAC	1	7.7
HDT	0.85	-0.28	*Polyelectrolytes*		
d43-18-MET	1	6.97	Chitosan	1.3[104]	3.1
d41-ET	1	6.95	pDADMAC	1	1.3

Knowing these values, it is possible to extract the volume fraction φ of a compound in an adsorbed layer, according to the equation $\varphi = (SLD_{solvent} - SLD_{layer})/(SLD_{solvent} - SLD_{dry})$ (as only one contrast was used in the experiments, the calculation is not possible if more than two components are in the layer). From the volume fraction, then, the surface excess Γ of the component, in terms of mol cm^{-2}, can be obtained as:

$$\Gamma = \varphi \cdot \tau \cdot \rho / MW$$

where τ is the thickness of the layer, ρ the density of the dry molecule and MW its molecular weight [105,106].

This is the general procedure used to fit and analyse NR data, but for those collected on the monochromatic instrument, a more complex procedure needed to be implemented.

The reason why the standard fitting protocol would not work is the over-illumination of the system. In fact, the correction applied during data reduction can only flatten the low Q region of the curve to account for beam intensity lost outside the sample, which is the only factor affecting reflectivity for e.g., the solid substrate in air. In an experiment at the solid/liquid interface, part of the beam not reflected by the area of interest interacts with the cell frame and contaminates the recorded reflectivity. This contribution varies along the Q range, as for sufficiently high angles of incidence only the central area of the sample is illuminated. This means that up to a certain Q value, two separate structures contribute to the NR signal, i.e., the sample in solution and the cell frame, while only the former is still present at larger Q, and so the two sections should be analysed separately. However, the extent to which this issue affects the data depends on the specific system.

This was proven by measurements of a thiol surface in GCMW at two different slit sizes (the one used for the experiments in paper I and III and a smaller size that ensured that no cell frame was illuminated even at low Q). For one measurement, a substrate presenting a titanium adhesion layer was mounted in the cell in Figure 3.2 B, while another measurement was done with the cell in Figure 3.2 A and a substrate with an adhesion layer of chromium. The obtained NR curves after reduction are in Figure 3.4 and Figure 3.5, respectively.

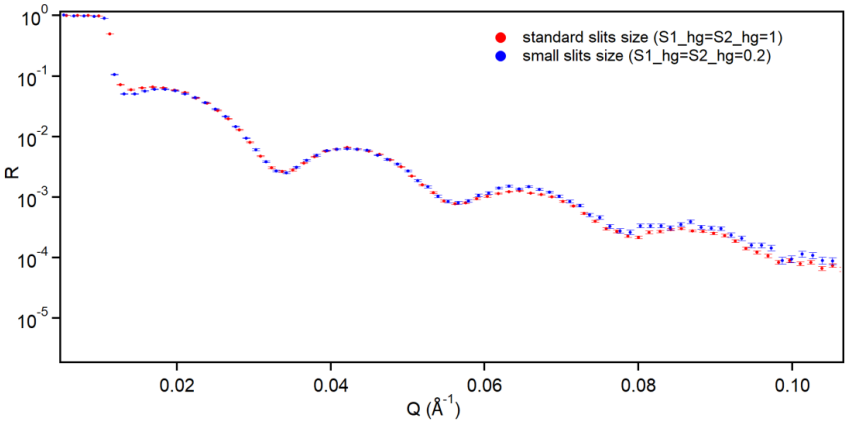

Figure 3.4 Test sample scans at 2 slits sizes as indicated in the graph. Sample surface: 50*50 mm², adhesion layer: titanium. Reproduced from paper I, ESI (CC-BY 3.0 license).

In the most commonly used setup (Figure 3.4), the contribution of the cell frame is hardly noticeable. Instead, the effect is clear when the second setup is used, see Figure 3.5.

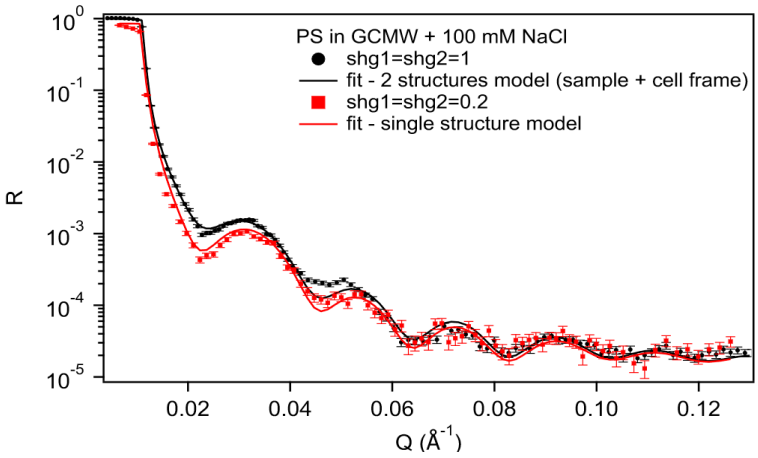

Figure 3.5 Test sample scans at 2 slits sizes as indicated in the graph. Custom solid/liquid cell, sample surface: 65*65 mm^2, adhesion layer: chromium. Reproduced from paper I, ESI (CC-BY 3.0 license).

This was the case for the experiments in paper I (the choice of this setup was made for reasons of material availability more than for a precise experimental design), but such a difference was unexpected, and its discovery took some time (and was prompted by the failure of fitting attempts by almost any available fitting tool). The separate contributions of the sample and the cell frame to the fit were simulated for the BT, MBT and PS samples, as shown in the ESI in paper I. The results for the BT surface, where the effect of over-illumination was particularly evident, is illustrated in Figure 3.6.

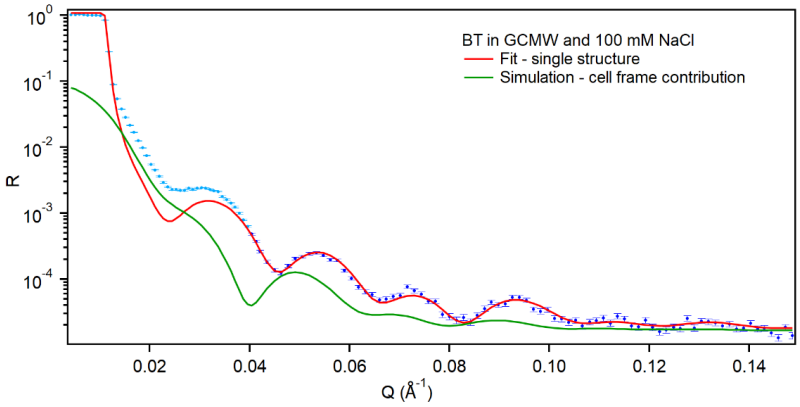

Figure 3.6 BT sample – dotted line: NR data, red solid line: simulation of sample structure, green solid line: contribution from cell frame (arbitrary scaled).

Figure 3.5 also shows a tentative fitting of the two curves using different models. To fit the red curve, whose reflectivity depends only on the area of interest, a standard slab model can be applied. For the black curve, the previous fit fails at low Q, where it is necessary to apply a two-structure model (this can be implemented in RefNX with the MixedReflectModel option). However, at high Q the two curves overlap, and the use of the two-structure model pushes the fitted curve above the experimental data. In fact, it can be noticed from Figure 3.6 that the simple (1-structure) model can fit the experimental data at $Q > 0.04$ $Å^{-1}$ (darker dots). At lower Q values (lighter dots), the contribution from the cell frame has to be included: the simulated green curve (which is composed of the same slab model for the substrate but facing a medium of SLD = 0 instead of GCMW) presents maxima aligned with the minima in the sample model, hence the effect on the collected data.

The implemented fitting procedure for the datasets in paper I is as follows:

- the curves for the thiol in pure solvent were separated in two sets ($Q < 0.04$ $Å^{-1}$ and $Q > 0.04$ $Å^{-1}$)
- the region at high Q was fitted with a simple slab model (differential evolution + MCMC analysis)
- the obtained parameters were used in the low Q region two-structure model to adjust the scaling factors of the structures
- if the fit at low Q was good (by eye), the characterized thiol layer was used to fit the subsequent adsorption steps with a similar procedure (see more details below)
- otherwise, the thiol layer was fitted at low Q and the obtained values checked at high Q, until self-consistent
- regarding the adsorption steps, for most of them the difference with the reflectivity curve of the pure thiol was visible at $Q > 0.04$ $Å^{-1}$, so, once checked that the structure at high Q was representative of the structure on the whole Q range, fitting of the adsorbed layers was performed at high Q (the results were anyway finally verified by simulating the obtained model on the whole Q range)
- in a few cases, notably chitosan, adsorption affected more the low Q region, so the curve at $Q > 0.04$ $Å^{-1}$ was fitted (with the two-structure model)

Specific modifications to the above procedure can be found in more detail in the ESI of paper I (e.g., the curve of the PS sample, as can be seen in Figure 3.5, had to be split at $Q = 0.05$ $Å^{-1}$ instead of 0.04 $Å^{-1}$).

3.3 Quartz-Crystal Microbalance

The QCM-D experiments were performed on a Q-Sense Analyzer (Biolin Scientific), located in the labs of the ILL/ESRF Partnership for Soft Condensed Matter (PSCM). The probes were gold-coated quartz crystals with resonance frequency of 5 MHz (OpenQCM). They were cleaned by UV/O_3 treatment (20 minutes) and sonication in solvents of increasing polarity (acetone – isopropanol – ethanol – Milli-Q water, for 10 minutes each), then blown dry with nitrogen. They were finally mounted in the QCM-D cell for thiolation *in situ* with a 1 mM solution of the appropriate thiol (or mixture) in absolute ethanol.

Before thiolation, a baseline in absolute ethanol was recorded, then for the adsorption experiments the solvent was switched to Milli-Q water containing 100 mM NaCl, recording again a baseline for about 10 minutes (if not stable, the system was allowed to equilibrate and the baseline restarted afterwards). Solutions were fluxed at a rate of 100 $\mu L\ min^{-1}$. If a plateau was not reached after about 15 minutes, the flux was stopped to incubate the system.

The systems studied by QCM-D were the pure PS and the mixed PS/MBT surfaces (see ESI in paper I and the *Materials and methods* section in paper II, respectively, for the full adsorption sequences).

The measurements were run in duplicate using two of the four available modules in the instrument. One additional measurement was performed to characterize the adsorption of SDS on pure MBT and compare it to the PS system (paper I).

Data analysis was tentatively carried out with the software QSense Dfind (Biolin Scientific), applying the available viscoelastic models (Smartfit and Broadfit). Due to the complexity of the performed experiments, the fitting was often suboptimal. For the data presented in paper II (adsorption of chitosan, oligomer and polymer, and SDS on a mixed MBT/PS surface), the software QTools (Biolin Scientific) was used. A one-layer Maxwell model [107] could be successfully applied to some datasets, but mostly the QCM-D data are discussed qualitatively.

3.4 Atomic Force Microscopy

AFM experiments were performed with a Bruker Dimension Icon instrument, in PeakForce Quantitative Nanomechanics (PF-QNM) mode [76]. Measurements were carried out in liquid using ScanAsyst Air tips (Bruker). The choice of this tip was made based on its low stiffness (0.4 $N\ m^{-1}$), to reduce deformation of the sample.

For the AFM measurements, the hair-mimetic models were prepared on template-stripped gold surfaces (Platypus Technologies), with a root mean square roughness of ~3 Å. The damaged hair models (PS, MBT/PS and 18-MEA thiol/PS) and the long-chain healthy hair model of pure 18-MEA thiol were

selected for the measurements. 2-3 images of 5 μm and 256 pixels were acquired, for at least three different spots on each surface. Samples were prepared in duplicate, and the resulting images were analysed in Gwyddion [108]. A background correction was applied, then particles were detected by thresholding (normally particles lower than 1 nm were excluded as within the error of the height of the clean surface), to define surface coverage and median of the height distribution for each image.

An attempt was made to determine the height of the thiol SAM: the layer was scratched by applying a high voltage (5 V), so that the depth of the hole visible in a topographic image acquired afterwards would be related to the thiol height. Unfortunately, heights of several nm were obtained from PS or PS/MBT surfaces, while the length of those molecules is below 1 nm. This suggests that the scratch affected the underlying gold layer, so these measurements were abandoned.

As mentioned in section 2.3.3, force curves can be obtained in PF-QNM mode. The idea was to compare the mechanical information to that extracted from QCM-D. An example of force curve is shown in Figure 3.7, recorded on a partially damaged hair model surface in the presence of chitosan, setting a trigger threshold (i.e., the difference between the maximum force reached in approach and the initial one sensed before contact) of 500 pN.

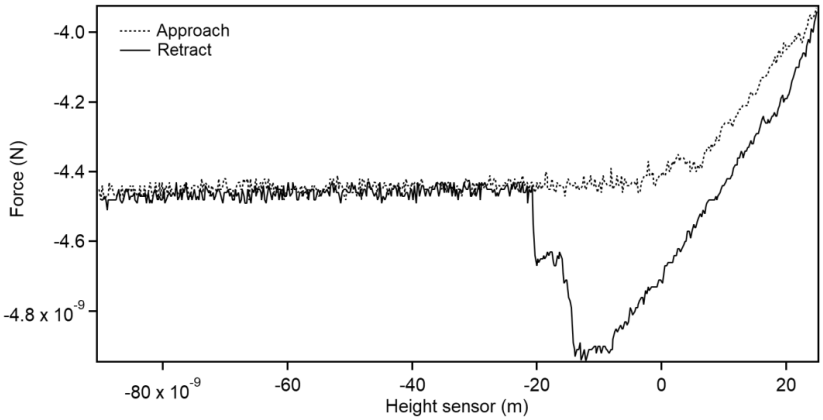

Figure 3.7 Force curve of a partially damaged hair model (50:50 MBT:PS) in the presence of chitosan.

The force starts increasing when the tip encounters the surface and deforms it until the preset force value. In the retract trace, the large negative deflection is due to the adhesion between tip and sample, which maintains the interaction until it is overcome by the restoring force of the cantilever [77]. However, results were poorly reproducible, probably because of the little layer thickness and the

influence of the substrate (and, in the presence of chitosan, its strong adhesion force that distorted retract traces), so only topographic images have been used to define the in-plane structure of adsorbed species and complement the results from NR.

4 Summary of results

The performed experiments can be broadly divided into two categories, according to the level of biomimicry of the surfaces, listed in section 3.1.

The short-chain models are based on commercially available thiols and reproduce just the outermost portion of the hair surface. There are four such models, two to represent a healthy hair surface (hydrophobic, with or without 18-MEA-like branch), one for a fully damaged hair surface (hydrophilic and negatively charged), and one to reproduce a partially damaged hair fibre (hydrophobic and hydrophilic patches). These models are described in paper I and II and illustrated in **Table 4.1**.

Table 4.1 Schematic representation of the short-chain hair-mimetic models

Healthy hair models		Damaged hair models	
Branched	Unbranched	Partially	Fully
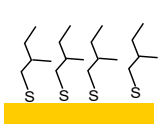	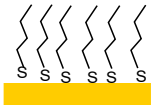	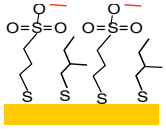	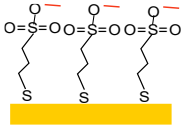
MBT	BT	MBT/PS	PS

The long-chain models required custom-made thiol derivatives of the hair lipids and introduced the effect of chain packing in the case of the healthy hair mimetics or mismatch in chain length in the case of partially damaged hair

models. Moreover, a mixed layer of branched and unbranched alkylthiols was added to the healthy hair models. **Table 4.2** illustrates this group of surfaces, and related experiments are in paper III and IV.

Table 4.2 Schematic representation of long-chain hair-mimetic models

Healthy hair models					Partially Damaged hair model
Branched		Unbranched		Mixed	
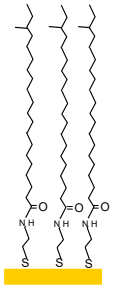	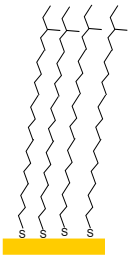	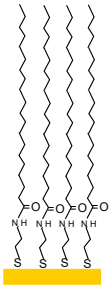	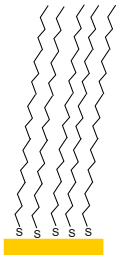	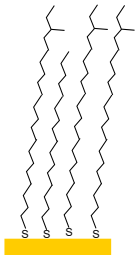	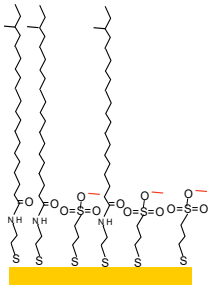
18-MEA thiol	18-MET	EA thiol	ET	18-MET/ HDT	18-MEA thiol/PS

Before the adsorption experiments, the structure of these models was investigated by NR, and the corresponding SLD profile was subtracted from those of the subsequent adsorption steps to isolate the contribution of the adsorbed species and highlight the layer of interest. A comparison between the general SLD profile and the subtracted one is shown in Figure 4.1. As described in the caption, the insert presents the region of the SLD profile relative to the thiol in pure solvent or in the presence of SDS. The negative peak just below x=0 corresponds to the thiol layer, which, being hydrogenous, has a SLD of -0.25 $*10^{-6}$ Å^{-2}. The SDS used in this example, instead, is deuterated and has an SLD of 6.2 $*10^{-6}$ Å^{-2}. The combination of these values with a relatively high interfacial roughness (ca. 10 Å) causes an apparent shift up of the peak of the thiol, which has no physical meaning as the thiol layer in the fitted model is unperturbed. This makes the comparison between successive adsorption steps less straightforward. To overcome this, the results are presented as difference spectra, which can then be interpreted in terms of the adsorbed species and their position relative to the surface.

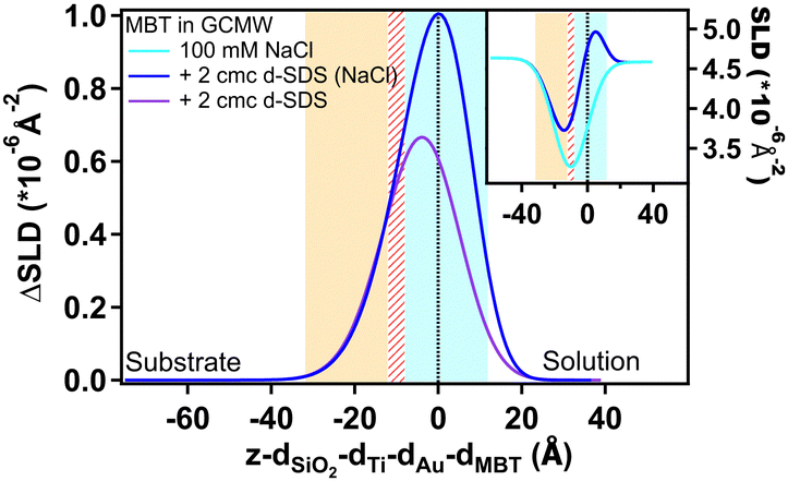

Figure 4.1 Depth profile, after subtraction of the substrate profile, of 2 cmc d-SDS adsorbed on MBT in the absence (purple line) and presence (blue line) of 100 mM NaCl (corresponding to 16 mM and 3 mM d-SDS, respectively). The light blue panel, centred at the dotted line at x = 0, indicates the MBT/d-SDS interface. The yellow panel indicates the Au/MBT interface. The widths are due to roughness, which causes an overlapping (striped area). The insert graph on the top right shows the SLD profile (zoom on the thiol + solution region), for the curve in the presence of NaCl (i.e., blue line), before subtraction of the thiol profile (cyan line); the x-axis is offset as in the main (thiol subtracted) graph. The thiol layer appears as an inverse peak due to its negative SLD. Reproduced from paper I (CC-BY 3.0 license).

Note on the characterization of the thiol layers: as mentioned in section 2.3, synchrotron GIXD measurements were tentatively performed at ESRF to obtain information about the organization of the thiol molecules in the SAM. Experiments were done using the short-chain models and an unexpensive long-chain SAM of 1-octadecanethiol (ODT), using gold-coated silicon chips (surface of 1*1 cm^2) as substrates. Two major problems were encountered. Firstly, the X-ray scattering contrast between thiol and air, or even more water, is very poor, which makes the signal of interest of low intensity. Secondly, the gold substrate was found to be not ideal for two reasons: it greatly increased beam damage (even if experiments were conducted under a beryllium dome with high attenuation of the X-ray beam), and its signal covered the thiol one due to its polycrystallinity. Literature studies report GIXD of thiol SAMs on gold, but they employ monocrystalline surfaces [109–111]. Instead, when measuring a ODT SAM on polycrystalline gold, the GIXD map is dominated by two rings, visible in Figure 4.2 (left panel), which are present already on the bare gold surface. For comparison, the expected signal would be like the one obtained from a test surface of octadecyltrichlorosilane (OTS) on silicon (on the right in the figure).

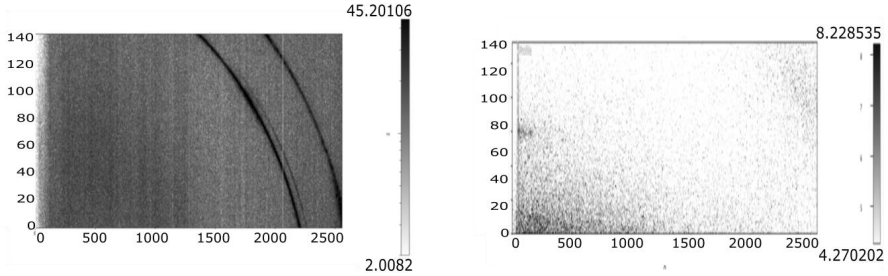

Figure 4.2 Left, GIXD of ODT on gold. Right, GIXD of OTS on silicon.

For this reason, the thiol SAM was characterized only by NR, and when possible AFM, measurements.

4.1 Short-chain hair-mimetic models

Starting with the short-chain models, the three pure thiol surfaces (MBT, BT and PS) are discussed in paper I, while the mixed MBT/PS surface is addressed in paper II. Paper I had a dual aim: not only studying adsorption on simple hair-mimetic surfaces, but also showing the feasibility of applying NR to such complex systems. Regarding the latter, as most of these experiments were conducted on a monochromatic reflectometer (SuperADAM, see **Table 3.1**), it was necessary to implement a fitting method that considered the over-illumination of the sample at small angles of incidence θ, as this could not be corrected for in the standard way due to a combination of factors related to the specific system and setup. The deployed fitting strategy is detailed in section 3.2.1.

Results from the fitting of NR data of the four short-chain models in pure solvent (GCMW containing 100 mM NaCl) are all compatible with the formation of a self-assembled monolayer of thickness ~7 Å [87]; in the case of the damaged hair models, the thiol layer shows on average about 10% hydration, while no water is associated to the healthy hair models.

For the general proof of concept in paper I, adsorption of SDS and oligomeric chitosan was studied, to compare the effects of the 18-MEA-like branch, surface charge, and sequential vs simultaneous injection of surfactant and polyelectrolyte. An example of the results obtained was shown in Figure 4.1: on the branched surface, adsorption of SDS was studied also in the absence of sodium chloride (the concentration of 100 mM NaCl used for all the other measurements was chosen to simulate the ionic strength of a shampoo formulation, that normally contains salt in the concentration range 100-500 mM [7,25]). In both cases, a (tilted) monolayer is formed (thickness 11 and 14 Å in

the absence and in the presence of salt, respectively – the length of the SDS molecule is 17 Å [112]). The surface excess that is extracted from the fitted parameters indicated the adsorption of 0.4 nmol cm^{-2} in the absence of salt and 0.5 nmol cm^{-2} in 100 mM NaCl.

A major result of paper I, though, was the unexpected adsorption of the anionic SDS molecules to the like-charge PS surface, shown in Figure 4.3.

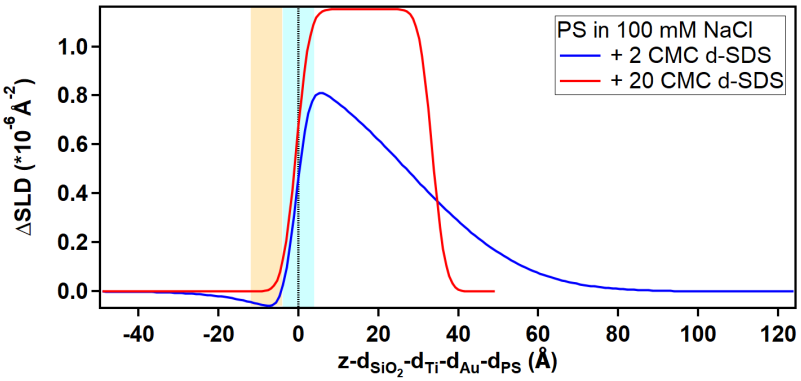

Figure 4.3 Depth profile, after subtraction of the substrate profile, of d-SDS adsorbed on PS (bulk d-SDS concentrations indicated in the figure). The blue panel, centred at the dotted line at x = 0, and the yellow panel on its left indicate, respectively, the PS/d-SDS and Au/PS interfaces with their associated roughness. Reproduced from paper I (CC-BY 3.0 license).

Some adsorption is visible already at 2 cmc SDS, although as a diffused and inhomogeneous layer, but the interesting result is the formation of a neat bilayer (thickness 34 ± 1 Å, i.e., twice the molecular length of dodecyl sulphate) from a 20 cmc solution. This prompted the performance of additional measurements, using hydrogenous SDS, to rule out the possibility of a specific effect of the deuterated sample used in the first experiment, and spiking the surfactant with dodecanol, to verify the hypothesis that this species was implicated in the observed anomalous behaviour. In fact, dodecanol is the hydrolysis product and a known contaminant of SDS [44], and its presence in the surfactants solutions was expected since the commercial SDS sample was not purified before use. This was chosen to keep the conditions as close as possible to the cosmetic application. As illustrated in paper I, the new NR experiments confirmed the first observations, which were in parallel also supported by QCM-D data (ESI of paper I). In the case of QCM-D data, quantitative results were more difficult to obtain, but they suggest the formation of a soft adsorbed layer of SDS on the sulphonate surface and a more rigid layer on the MBT surface, which agrees with the different hydration levels deduced from the NR data. The explanation for this unexpected adsorption is a combination of two factors. On the one hand,

sodium ions bind to the surface neutralizing the sulphonate charge and mediating SDS adsorption to it (sodium ions are present in a concentration of at least 130 mM: 100 mM from NaCl and 30 mM from SDS, plus the counterions of PS itself). On the other hand, as deuterated dodecanol was observed to be enriched on the surface compared to the bulk solution, there may be a preferential partitioning due to the penalty of adsorption of dodecyl sulphate ions on the negatively charged surface. Those effects are summarized in Figure 4.4.

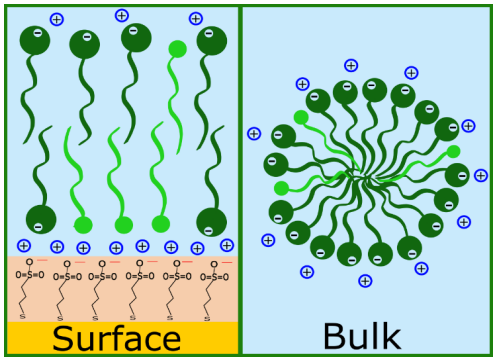

Figure 4.4 Schematic drawing of dodecanol partitioning on the PS surface and in a micelle in the bulk. Light green molecules represent dodecanol, bottle green ones with negative charge are dodecyl sulphate, blue circles with positive charge represent sodium ions. Reproduced from paper I (CC-BY 3.0 license).

The same SDS bilayer structure is observed when SDS is introduced in complex with chitosan oligomer (at a concentration of 20 cmc surfactant and 100 ppm polyelectrolyte, which corresponds to a cosmetically relevant ratio – see section 2.2). In this case, an additional layer of 65 ± 10 Å is visible, that extends from the SDS bilayer towards the bulk and is composed of both SDS and chitosan. A similar two-layer structure is observed on the other short-chain surfaces but presenting an SDS *monolayer* and a second layer, several tens of Å thick, of pure (hydrated) chitosan. The results on these short-chain models suggest that the methyl branch does not affect the interaction properties of the surface, but later results show that this is due to the different packing of these thiols compared to long-chain ones, as will be discussed further on in paper III. Also, results on the mixed MBT/PS surface (partially damaged hair model) show an intermediate adsorption behaviour, where the interaction with the surfactant is determined by the hydrophobic patches and chitosan association is enhanced as on the pure sulphonate surface. An example of the results to illustrate this behaviour is in Figure 4.5; for comparison, results for the pure constituents separately are in Figure 4.6 and Figure 4.7.

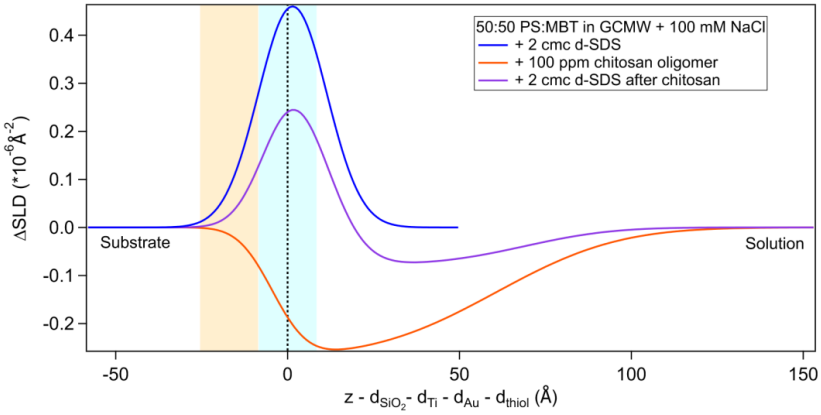

Figure 4.5 Subtracted SLD profiles of 2 cmc d25-SDS adsorbed on 50:50 MBT:PS, before and after injection of chitosan oligomer. For comparison, the profile corresponding to pure chitosan is added. The zero of the x-axis is at the thiol/d25-SDS interface, whose roughness is indicated by the blue panel. Similarly, the yellow panel on the left represents the Au/thiol interface with its associated roughness. Reproduced from paper II.

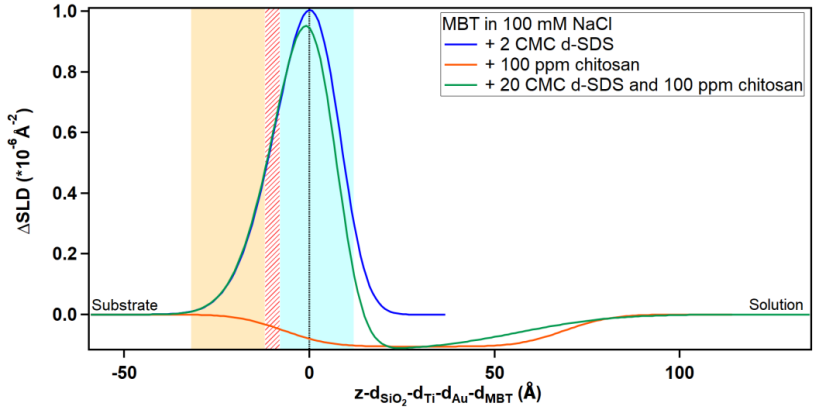

Figure 4.6 Depth profile, after subtraction of the substrate profile, of adsorbed species on MBT as indicated on the graph. The blue panel, centred at the dotted line at x = 0, indicates the MBT/adsorbed layer interface. The yellow panel indicates the Au/MBT interface. The widths are due to roughness, which causes an overlapping (striped area). Reproduced from paper I (CC-BY 3.0 license).

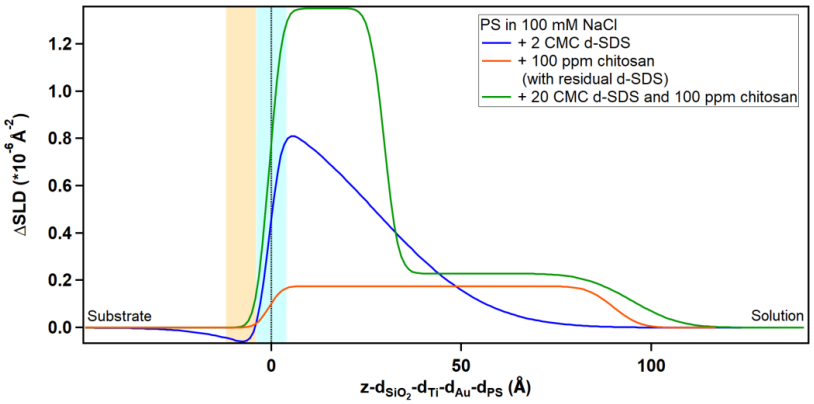

Figure 4.7 Depth profile, after subtraction of the substrate profile, of adsorbed species on PS as indicated on the graph. The rinsing step before introduction of chitosan left a residual layer of deuterated species that caused the ΔSLD of chitosan to be positive. The blue panel, centred at the dotted line at x = 0, and the yellow panel on its left indicate, respectively, the PS/adsorbed layer and Au/PS interfaces with their associated roughness. Reproduced from paper I (CC-BY 3.0 license).

The SDS monolayer has the same thickness as on pure MBT, but its surface excess is only 0.22 nmol cm^{-2}, compatible with the presence of hydrophobic moieties on only half of the surface. A subsequent injection of 20 cmc SDS did not lead to the formation of a bilayer as on pure PS, but only to a slight increase of the surface excess to 0.25 nmol cm^{-2}. Instead, chitosan adsorption increased, likely due to a favourable electrostatic interaction with sulphonate groups. Once again, in the presence of both surfactant and polyelectrolyte on the surface, two layers can be distinguished. Comparing, in the three cases, the ΔSLD values of the profile for the SDS/chitosan mixture with those of the two components adsorbed separately, it is clear that the association between the adsorbing species is stronger in the case of the damaged hair models than on the pure MBT surface. The purple profile shown in Figure 4.5 refers to the sequential injection of the two species, however a subsequent injection of a premixed SDS/chitosan complex gave similar results, with the difference that the thickness of the first layer increased to 23 Å. This is not enough to define a bilayer, but is larger than a monolayer, suggesting interaction of the surfactant molecules with both the surface and the adsorbed chitosan.

In paper II, adsorption of chitosan is further studied by comparison of the 3 kDa chitosan (oligomer) with a 27 kDa one (polymer), by NR and QCM-D. The effect of the molecular weight on the interaction between chitosan and the partially damaged hair mimetic surface is illustrated in Figure 4.8.

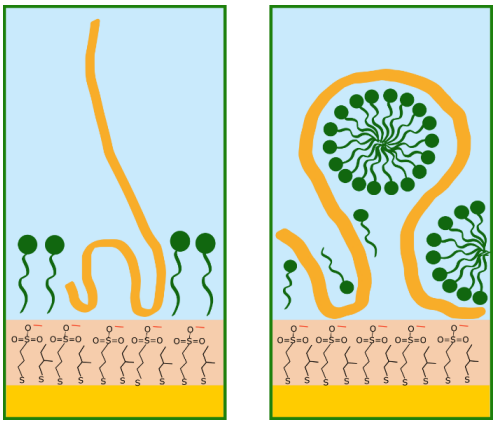

Figure 4.8 Schematic drawings of SDS (green) adsorbed after chitosan (orange): left, oligomer; right, polymer. Reproduced from paper II.

Basically, in the presence of the polymeric chitosan, one compact layer, 29 (± 4) Å thick, is observed instead of the two layers of thickness 13 (± 2) and 60 (± 10) Å, resulting from the fitting of the oligomer data (the larger error on the second slab is due to the lack of contrast – i.e., to the closeness of the SLD value of the layer to that of the bulk). Results from QCM-D measurements qualitatively agree with NR, as the frequency (and dissipation) shift caused by adsorption of SDS after chitosan polymer are better interpreted as changes in the viscoelastic properties of the layer rather than an increase in layer thickness. This is compatible with the formation of a compact layer of associated components, although the thickness values cannot be directly compared between the two techniques (those obtained by QCM-D are significantly larger due to the hydration water being detected together with the adsorbed molecule of interest). Successive rinse suggests for both methods that the surfactant is preferentially removed.

Another major finding of paper II was the use of AFM to determine the in-plane structure of the adsorbed aggregates. In fact, NR has the unique ability to separate contributions based on the different SLD of hydrogenous and deuterated species, but it averages information in-plane. For example, the layer formed by pure chitosan on the mixed MBT/PS surface (Figure 4.5) contains 80% solvent, but this could be due to either a homogeneously hydrated layer or the adsorption of chitosan as separate aggregates spread on the surface. AFM images revealed that the latter is true, as shown in Figure 4.9. The figure is composed of two AFM images, acquired on different spots of the same sample: this indicates that separate aggregates are present, but their distribution is not homogeneous.

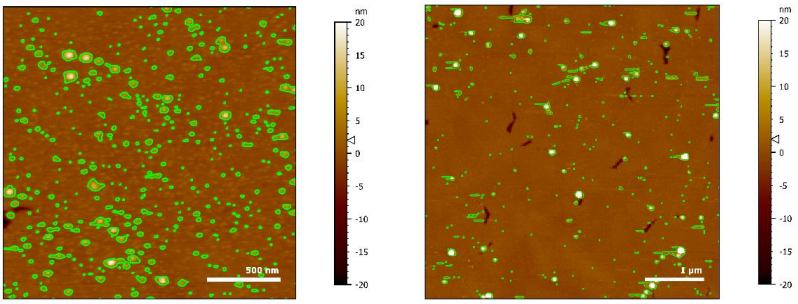

Figure 4.9 AFM images of chitosan oligomer adsorbed on 50:50 MBT:PS surfaces at two different positions. The detected particles are coloured in green. Reproduced from paper II.

4.2 Long-chain hair-mimetic models

The long-chain models were designed primarily to verify how the chain packing would affect adsorption and how results would differ from the short-chain models, but they showed some unexpected peculiarities in the thiol layer structure.

A layer different from a conventional SAM was obtained for the 18-MEA and EA thiols, as detailed in the ESI of paper III, while the use of deuterated thiols in paper IV revealed the presence of nanobubbles or a depletion layer on the hydrophobic surfaces. Both results are better explained below, while adsorption of surfactants and polyelectrolytes is described afterwards.

Regarding 18-MEA and EA thiol surfaces, as it can be seen in **Table 4.2** they not only present the correct C20 chain but also maintain the C=O feature of 18-MEA (albeit in the form of an amide) to increase the biomimicry of the system. This had unforeseen consequences on the structure of the model: the thickness of the layer in pure solvent exceeded that expected for a monolayer of 18-MEA, which according to the literature is 20–26 Å [113] (the extended chain length is ca. 30 Å). The fitted value was instead about 40 Å and decreased to 28-30 Å after exposure to surfactant solutions above the cmc (a few Å more than the literature values are compatible with the presence of the ethyl spacer used to convert the fatty acid to a thiol). In paper III this discussion is confined to the ESI to better focus on the adsorption to the hydrophobic thiol layers, but in fact the majority of effort was directed at understanding the anomalous behaviour displayed by these samples.

The experiments were performed in two different beam times (the experimental sequences are in the *Materials and methods* section of paper III). NR fitting

results were particularly interesting in the case of the interaction with the cationic surfactant CTAC, shown in Figure 4.10 and Figure 4.11.

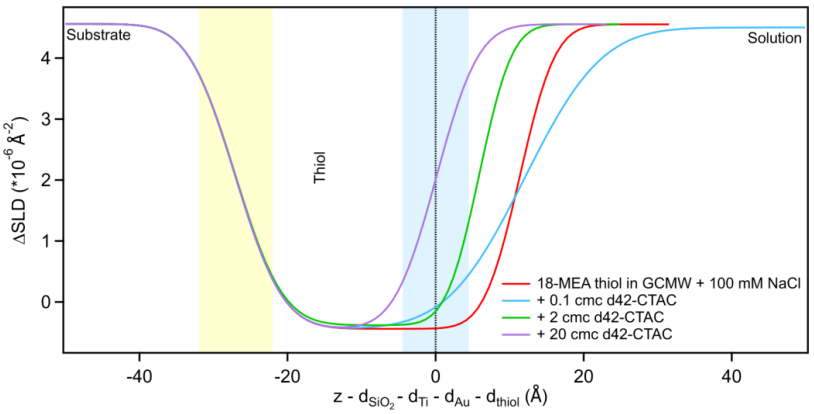

Figure 4.10 Depth profiles relative to the 18-MEA thiol in the presence of d42-CTAC, at the concentrations indicated in the graph. The yellow and blue panels represent the Au/thiol and thiol/solution interfaces, respectively, with associated roughness. The zero level on the x-axis has been set at the "clean" thiol/solution interface. Reproduced from paper III (ESI).

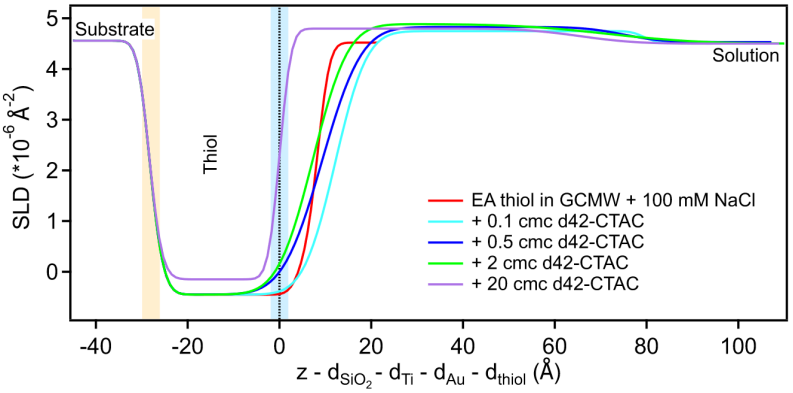

Figure 4.11 Depth profiles relative to the EA thiol in the presence of d42-CTAC, at the concentrations indicated in the graph. The yellow and blue panels represent the Au/thiol and thiol/solution interfaces, respectively, with associated roughness. The zero level on the x-axis has been set at the "clean" thiol/solution interface. Reproduced from paper III (ESI).

In both cases, the decrease in thickness at increasing surfactant concentrations is evident, but so is the different adsorption behaviour.

On the 18-MEA thiol surface, a modification of the thiol layer (increase in the roughness of the thiol/solution interface) is already visible at a CTAC concentration of 0.1 cmc, while no variation is observed in the SLD value. This suggests that part of the original thiol layer is removed, and the remaining molecules rearrange preventing significant changes in the layer density. The removed molecules would be free 18-MEA thiol intercalated in between the covalently bound chains, similar to the model described in a recent publication by Wang *et al.* [113] (meaning this is indeed a good representation of the hair fibre). Strictly, as mentioned in the ESI of paper III, another explanation is possible, i.e., that some surfactant molecules do bind to the thiol surface, intercalating between residual free chains, but their contribution is hidden by a compensation of the SLDs (the surfactant being deuterated and the thiol hydrogenous) to a total value that is contrast-matching the bulk solution (whose SLD is 4.55 $*10^{-6}$ $Å^{-2}$). This would be possible at a ~3:2 CTAC:18-MEA thiol ratio. The two mechanisms may be occurring simultaneously, which makes the quantitative interpretation of results from the subsequent steps difficult. A schematic drawing of the two scenarios is in Figure 4.12 (please note that this is over-simplified for illustrative purposes).

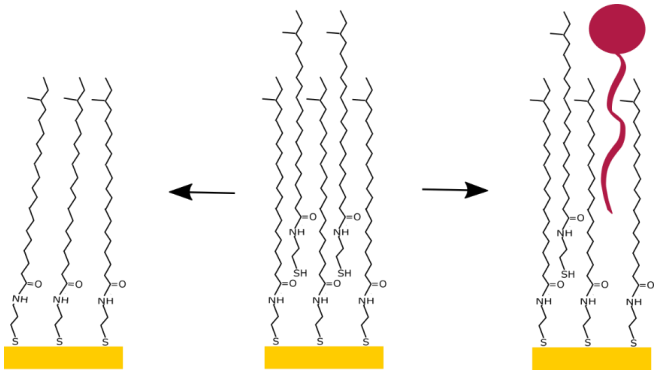

Figure 4.12 Simplified representation of the possible scenarios for the interaction of the 18-MEA thiol surface with CTAC. The hypothesised structure in water is illustrated in the centre. Left, "clean" monolayer after removal of free chains by the surfactant. Right, partial removal of free thiol and intercalation of CTAC (magenta).

The description of the NR results regarding the straight-chain EA thiol is more complicated. An adsorbed layer is visible at low surfactant concentrations, whose SLD is slightly larger than the bulk and whose thickness corresponds to ca. 65 Å. A CTA ion has a length of 22 Å [114], so the fitted slab would be even

larger than a bilayer. The SLD value indicates that the layer contains predominantly deuterated material but mixed to a significative amount of hydrogenous species, which may be explained by a high level of hydration or, more likely considering the thickness, by free thiol molecules associated with adsorbing CTAC. Differently from the branched thiol, the thickness here does not significantly change up to 2 cmc surfactant, even though the interfacial roughness increases. At 20 cmc, the thickness decreases to the same value as that of the 18-MEA thiol at the same CTAC concentration, but unlike that, the variation in thickness is accompanied by an increase in the layer SLD, which suggests a lower chain density in the layer (less tightly packed monolayer).

The different behaviour of the 18-MEA and EA thiols led to the hypothesis that the original structure of the unbranched thiol layer was formed by free EA molecules intercalating (as on 18-MEA) but aligned in the opposite direction of the bound chain, with the thiol moiety towards the bulk (see Figure 4.13). This would form a hydrophilic rather than hydrophobic surface and modify the interaction with the surfactant.

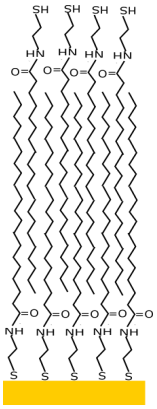

Figure 4.13 Schematic representation of the hypothesised structure of the EA thiol layer in water.

A simulation of such a structure, as shown in the ESI of paper III, follows well the NR data of the EA thiol in pure solvent, but the fit would not converge, probably due to correlations between the increased number of fitting parameters, so this hypothesis, while highly probable, cannot be *proven* unambiguously from the current data.

Regarding the 18-MET and ET surfaces (paper IV), the structures were simplified compared to the previous 18-MEA and EA thiols, by reducing the carboxylic group to have simple alkylthiols. Both molecules were deuterated, to explore different contrasts to study adsorption, and particularly to test a more

accurate model of a healthy hair surface, composed by the branched C20 (18-MET) and an unbranched C16 (HDT) species at a ratio of 70:30. This thiol ratio, if 18-MET is deuterated and HDT is hydrogenous, forms a layer whose SLD value contrast-matches gold, highlighting the contributions from the adsorbed layer(s).

Characterization of these thiols was then done both in pure H_2O and in GCMW with 100 mM NaCl. Results for d43-18-MET and d41-ET, both in H_2O and the former also in GCMW, are in Figure 4.14.

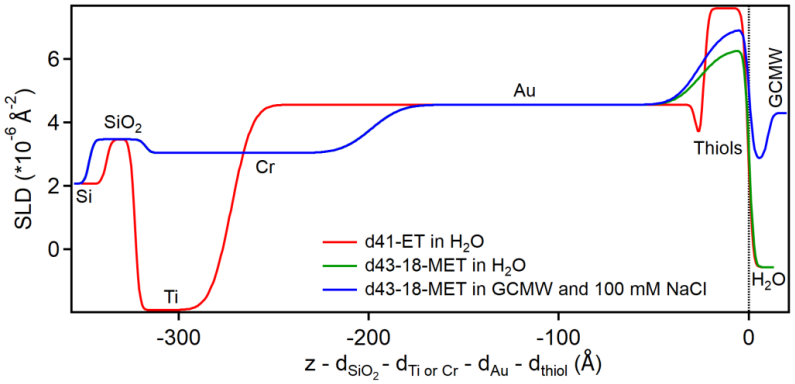

Figure 4.14 SLD profiles from fitting of NR data of d41-ET and d43-18-MET in the solution indicated in the graph. The zero on the x-axis corresponds to the thiol/solution interface. The difference between the two systems is mostly due to the different substrate. Reproduced from paper IV.

The first obvious feature of the profiles in Figure 4.14 is the difference between the gold-coated substrates, which affects also the appearance of the bound thiol layer. In fact, the higher roughness of the gold layer functionalized with d43-18-MET makes the region of the thiol layer less defined than the corresponding profile of d41-ET. However, a major observation from these results is the appearance of a negative peak, ca. 10 Å thick, just above the thiol/solution interface. Its presence was hidden in pure water because of the lack of scattering contrast. It is compatible with the presence of nanobubbles, or a depletion layer, due to the hydrophobicity of the surfaces [115–117], and disappears after exposure to the surfactant solutions. In light of this result, another explanation could be possible for the unexpectedly thick hydrogenous layer observed on the 18-MEA and EA thiol surfaces previously discussed. However, the SLD value of the depletion layer defined on d43-18-MET is 2.86 *10^{-6} Å^{-2}, compatible with a low-density solvent layer as described by Schwendel *et al.* [117]. Instead, the profiles in Figure 4.10 and Figure 4.11 are more consistent with the presence of a compact

layer (of hydrogenous material). While this does not completely rule out the presence of nanobubbles on those other surfaces, nonetheless the presence of additional (free) thiol molecules intercalated to the bound ones is the main factor causing the previously observed structure.

Regarding the mixed d43-18-MET/h-HDT and PS/18-MEA thiol surfaces, fitting of the NR data in pure solvent allowed the calculation of the thiol ratio on the surface, which, as mentioned in section 3.1, does not always correspond to the ratio in the prepared solution. Different behaviours were observed for the two mixtures. In the case of the more biomimetic healthy hair model (i.e., d43-18-MET/h-HDT), the thiol slab could not be distinguished from the underlying gold layer due to poor contrast, as described in paper IV. This indicates that, despite the difference in chain length, the thiols adsorb with similar affinity to the surface and so the ratio of bound thiols resembles the ratio in solution.

In contrast, for the mixed PS/18-MEA thiol surface, obtaining the desired ratio on the surface was not straightforward. Initially, two samples were prepared using a 50:50 thiol solution, as was done for the corresponding short-chain model. The longer 18-MEA chain, however, has a stronger drive to adsorption, so that NR showed, for the two samples, a complete 18-MEA thiol layer in one case and a 19:81 PS:18-MEA thiol ratio on the surface in the other case.

Based on independent X-ray photoelectron spectroscopy measurements on ODT/PS samples (shown in the ESI of paper III), the solution ratio was increased to 80:20 PS:18-MEA thiol. With this recipe, the surface ratio extracted from the SLD value of the thiol layer corresponds to 64:36 PS:18-MEA thiol.

The mixed PS/18-MEA thiol surface also revealed interesting structural features when studied by AFM. The topographical images show some homogeneous regions, as that presented on top right of Figure 4.15, but, interestingly, some patchy regions are also observed, indicating that the two species do not completely mix on the surface. The height of the features in the graph, of ~2 nm, is compatible with the mismatch in chain length between the two thiols. The domains of long-chain thiols have a size of about 1 μm. Such heterogeneity provides good biomimicry.

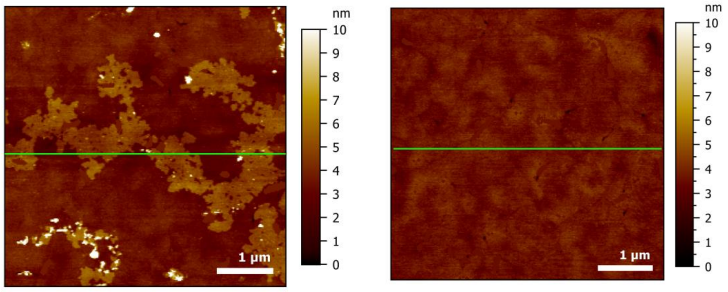

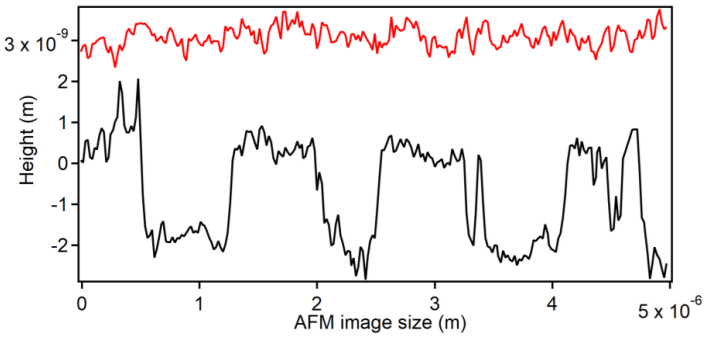

Figure 4.15 Example of AFM images (top) and corresponding profiles (bottom) (extracted along the green lines on the AFM images) relative to a 50:50 PS:18-MEA thiol sample in water plus 100 mM NaCl. The image on the left shows a region with patches of different height (black profile), the one on the right a more homogeneous region of the same surface (red profile). Reproduced from paper III.

This organization in domains is important to interpret the SLD profiles of surfactant adsorption to this partially damaged hair model. As an example, the profiles in the presence of SDS are presented in Figure 4.16.

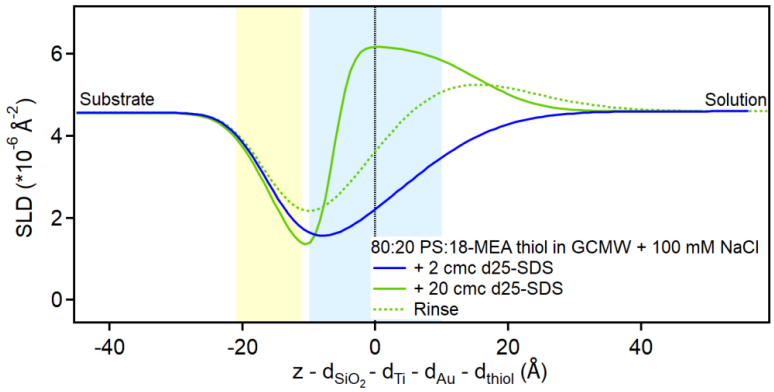

Figure 4.16 Depth profiles of the partially damaged hair model in the presence of d25-SDS at the concentrations of 2 and 20 cmc and following rinse. The yellow and blue panels represent the Au/thiol and the thiol/solution interfaces, respectively, with associated roughness. The zero value on the x-axis corresponds to the thiol/solution interface in pure solvent. Reproduced from paper III.

Unlike the other systems, in this case the fitted SLD profile is shown without subtraction, because the more complex structure of the thiol layer may

introduce artefacts in the difference profiles, as discussed in the ESI of paper III. The low concentration (2 cmc) of SDS does not significantly modify the SLD profile of the biomimetic layer, which has an average thickness of 15 Å, while at a higher concentration (20 cmc), a peak of deuterated material (higher SLD than the bulk) is clearly visible, in the region initially referred to the thiol, that is now confined to a 9 Å thick layer. The thickness (21.8 ± 0.7 Å) and shape of the adsorbed layer suggest that it may be due to a combination of two mechanisms. On one side, it can adsorb hydrophobically to the 18-MEA thiol, perhaps intercalating between the loosely packed chains, and on the other side it can form a bilayer on the hydrophilic patches, similar to what was observed in paper I (Figure 4.4). This scenario is illustrated in Figure 4.17.

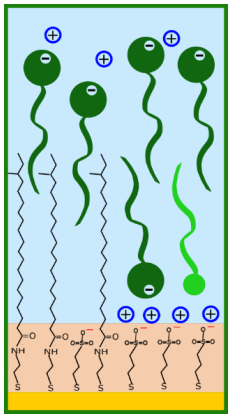

Figure 4.17 Schematic drawing showing the two possible mechanisms for adsorption of SDS on the two patches of the partially damaged hair model. Blue circles: sodium ions; bottle green molecules: SDS; light green molecule: dodecanol. Reproduced from paper III.

As on the pure sulphonate surface, a preferential partitioning of dodecanol likely occurs on the negatively charged patches. The interactions taking place at the boundary of two domains, in addition, may be particularly strong and drive the adsorption of subsequent molecules. This would explain why such a structure was not observed on the corresponding short-chain mixed system illustrated in paper II (Figure 4.5): the absence of the anchor points offered by the chain mismatch might have caused, in that case, a simple hydrophobic adsorption on the MBT molecules to dominate the surface properties. A similar scenario can also explain data in the presence of the cationic CTAC (see paper III), which, at a concentration of 20 cmc, adsorbs as a bilayer of 40 (±3) Å (in this case, the cationic headgroup would interact with the sulphonate patches, displacing

sodium ions), whose SLD indicates the presence of both deuterated and hydrogenous species on top of a 9 Å thick layer of pure thiol.

Besides the interaction with surfactants, a comparison between a natural and a synthetic polymer (i.e., the polymeric form of chitosan and pDADMAC, respectively) is described in paper III.

Results for the partially damaged hair model are in Figure 4.18. As on the other surfaces, adsorption of chitosan does not lead to a visible slab, due to the expected high hydration level [52,70,81,118] and to residues from the previous adsorption steps (and therefore related scattering contrast arguments). However, the presence of chitosan is revealed by the subsequent increase in surfactant (SDS) adsorption.

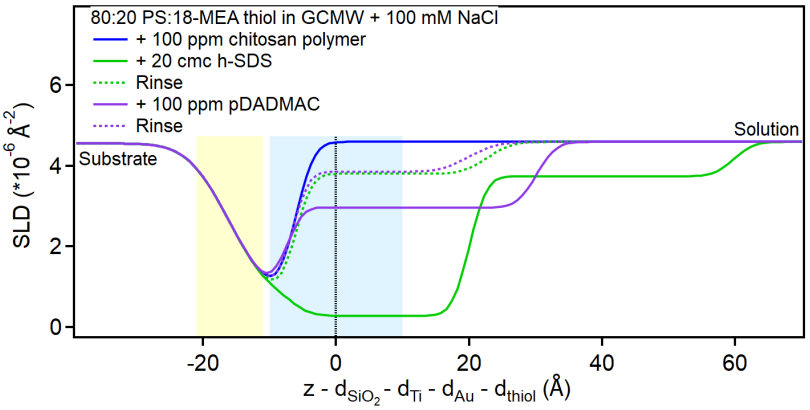

Figure 4.18 Depth profiles of the partially damaged hair model in the presence of chitosan polymer or pDADMAC and SDS at the concentrations indicated in the graph. The yellow and blue panels represent the Au/thiol and the thiol/solution interfaces, respectively, with associated roughness. The zero value on the x-axis corresponds to the thiol/solution interface in pure solvent. Reproduced from paper III.

As was observed in paper II on the short-chain mixed model, SDS is likely to be preferentially removed so that the layer observed after rinsing would be formed by irreversibly adsorbed chitosan with residual associated SDS/dodecanol. The subsequent introduction of the synthetic polymer pDADMAC is clearly defined by the appearance of a layer of lower SLD; interestingly, though, the residual layer after rinsing resembles the one before injection of chitosan, which suggests that pDADMAC might have been loosely adsorbed. Results related to a fully sulphonate surface do not support nor refute this finding, as in the presence of both polymers the low contrast to the bulk solution does not allow the drawing of unambiguous conclusions. In fact, the increased adsorption of SDS after each

polymer step indicates the presence of irreversibly adsorbed polymer, but it is not possible to define whether the layer is composed of only chitosan or of pDADMAC too (see Figure 15 in paper III). This was unexpected as quaternary ammonium polymers are known to have a conditioning effect due to their ability to bind to damaged hair fibres. This point may need further studies to be clarified, but the presented results suggest that the polymeric chitosan might have a stronger affinity than the synthetic pDADMAC for the hydrophilic patches of a damaged hair surface, which is an interesting finding from a cosmetic perspective, considering the implications for sustainability.

Instead, the adsorption of pDADMAC seems irreversible on the 18-MEA thiol surface, as shown in Figure 4.19.

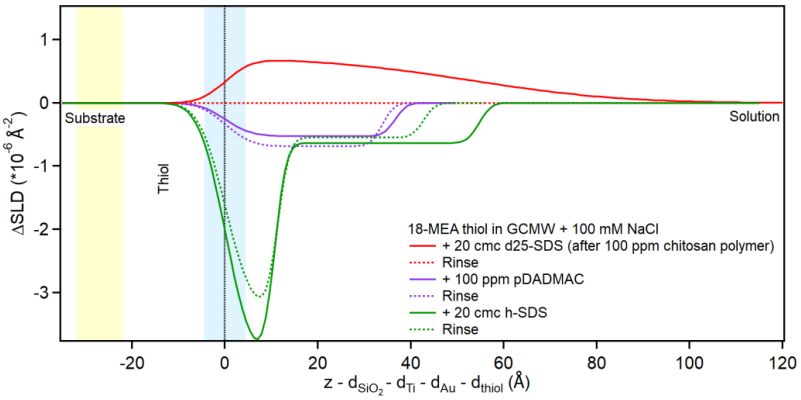

Figure 4.19 Depth profiles of a healthy hair model in the presence of chitosan polymer or pDADMAC and SDS at the concentrations indicated in the graph. The yellow and blue panels represent the Au/thiol and the thiol/solution interfaces, respectively, with associated roughness. The zero value on the x-axis corresponds to the "clean" thiol/solution interface. Reproduced from paper III.

Two major features can be noted in comparing the SLD profiles in Figure 4.19 with those in Figure 4.18. Firstly, as mentioned, pDADMAC seems to adsorb irreversibly, as the profile does not change significantly after rinsing. Secondly, the shape of the SLD profiles in the presence of 20 cmc SDS (green solid lines) once again confirms the mechanism of interaction of the anionic surfactant on the two types of surfaces: an hydrophobically adsorbed monolayer on the 18-MEA thiol surface, and a bilayer on the hydrophilic patches of the mixed thiol model. (The SLD profiles are in fact reminiscent of those presented in Figure 4.6 and Figure 4.7 for the short-chain biomimetic models.)

A strong interaction of the branched thiol surface with polyelectrolytes was confirmed by two more experiments, one on a similar 18-MEA thiol model in

the presence of SDS and the oligomeric form of chitosan (paper III), and the second one on the deuterated 18-MET surface (paper IV). Both experiments revealed the presence of an irreversibly adsorbed oligomer residue, as shown for example in Figure 4.20.

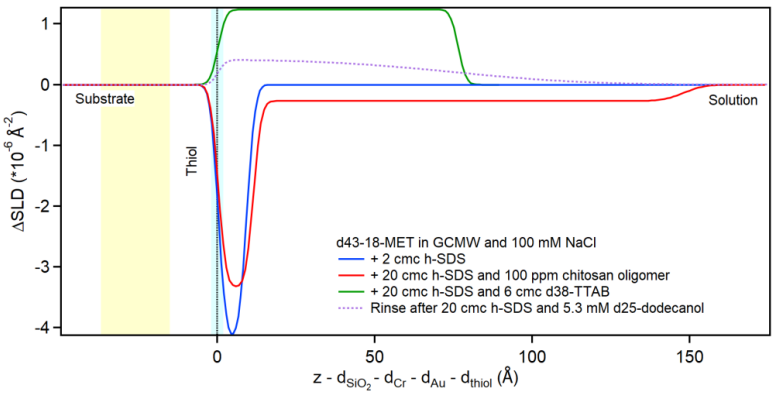

Figure 4.20 Subtracted SLD profiles of d43-18-MET in GCMW and 100 mM NaCl, in the presence of the species indicated in the graph. The yellow and blue panels represent, respectively, the gold/thiol and thiol/solution interfaces with associated roughness. x=0 indicates the thiol/solution interface. Reproduced from paper IV.

As observed already in Figure 4.19, the presence of the oligomeric chitosan affects the adsorption of surfactants in subsequent steps. The mixture of SDS and TTAB (at a ratio that simulates that of primary anionic and secondary cationic surfactants in shampoo formulations) adsorbs in a 76 (±1) Å thick layer, clearly too large to be pure surfactant, so it is best interpreted as (mainly) TTAB molecules (due to the largely positive SLD indicative of deuterated material) interacting with irreversibly adsorbed chitosan. Likewise, the final rinse performed on the system reveals that a thick layer is still adsorbed. This final rinse followed the injection of an SDS solution spiked with dodecanol, as done on the damaged hair model in paper I, to verify that no preferential partitioning is in this case observed. Results (in the ESI of paper IV, with rather large error bars) *suggest* the adsorption of a layer of mainly hydrogenous material, compatible with the higher proportion of SDS in solution.

Instead, the hypothesis was proven on the unbranched surface. The same adsorption sequence resulted in a very different interaction with the surface, as illustrated in Figure 4.21.

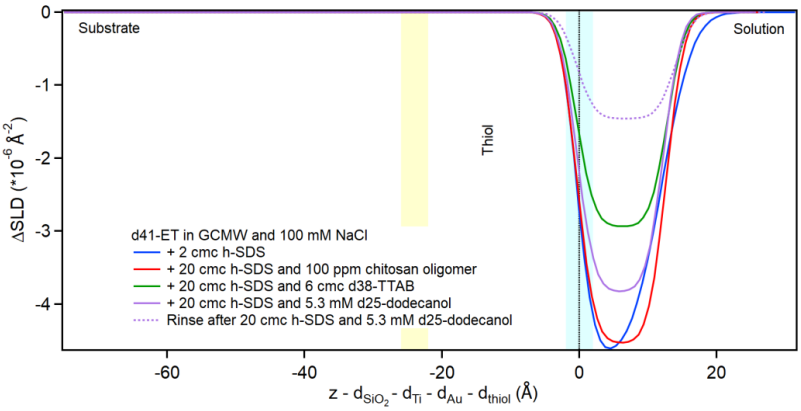

Figure 4.21 Subtracted SLD profiles of d41-ET in GCMW and 100 mM NaCl, in the presence of the species indicated in the graph. The yellow and blue panels represent, respectively, the gold/thiol and thiol/solution interfaces with associated roughness. x=0 indicates the thiol/solution interface. Reproduced from paper IV.

Adsorption on the unbranched thiol surface is strikingly dominated by the interaction with the surfactant. At each step, a defined monolayer is obtained, whose SLD reflects that of the molecule or complex in solution, so no specific effect of dodecanol is observed, besides a small propensity to be resolubilized after adsorption (the SLD of the adsorbed layer increases after rinsing, indicating that more deuterated material is left on the surface).

In particular, the SDS/chitosan complex also leads to a pure monolayer of surfactant, differently to Figure 4.20. The same outcome was obtained on the EA thiol surface in the presence of SDS and chitosan oligomer (ESI of paper III). Together, the results reported in paper III and IV lead to conclude that, irrespective of the packing constraints given by the presence of the amide bond (that simulates the thioester moiety on the surface of hair), it is the antepenultimate bond of 18-MEA that affects the interaction of the biomimetic surface with the simplified formulations.

The methyl branch of 18-MET seems to have a specific effect on the adsorption of chitosan, as the pure HDT surface showed a similar behaviour to d41-ET (no evidence of chitosan adsorption), while an extended layer, compatible with chitosan molecules, is visible on the mixed healthy hair model (70:30 18-MET:HDT system), similarly to pure 18-MET.

The SLD profiles relative to the experiment performed on the mixed healthy hair mimetic surface are in Figure 4.22.

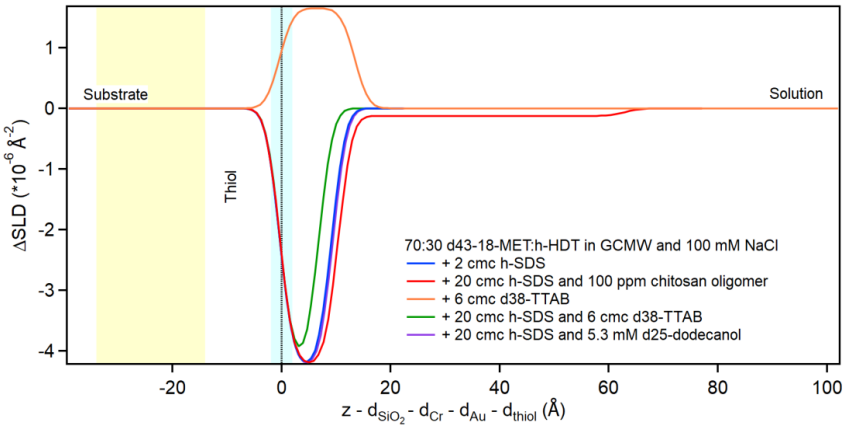

Figure 4.22 Subtracted SLD profiles of 70:30 d43-18-MET:h-HDT in GCMW and 100 mM NaCl, in the presence of the species indicated in the graph. The yellow and blue panels represent, respectively, the gold/thiol and thiol/solution interfaces with associated roughness. x=0 indicates the thiol/solution interface. Reproduced from paper IV.

In the presence of the SDS/chitosan oligomer complex, a second extended layer is visible above the surfactant monolayer, further away from the surface, as seen already in Figure 4.20. However, the interaction here seems to be weaker than on pure 18-MET, as subsequent adsorption steps do not show association to residual chitosan. A schematic representation of the different adsorption scenarios of the SDS/chitosan complex on the three biomimetic surfaces just discussed is in Figure 4.23.

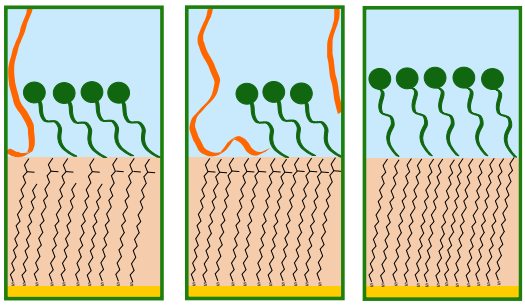

Figure 4.23 Schematic representation of the adsorption layers obtained exposing the different surfaces to a 20 cmc h-SDS (green molecules)/100 ppm chitosan oligomer (orange lines) complex. Left, 70:30 d43-18-MET:h-HDT. Centre, d43-18-MET (more chitosan is detected). Right, d41-ET (as example of unbranched surface - the adsorption is dominated by SDS). Reproduced from paper IV.

5 Conclusions

In the context of increasing the sustainability of cosmetic formulations, a fundamental understanding of the interaction and adsorption processes occurring at the hair or skin surfaces is crucial, to guide the design of new products incorporating more eco-respectful ingredients and processes.

This project specifically dealt with hair, and thus shampoo formulations, investigating the interaction behaviour of hair-mimetic surfaces. The use of biomimetic models instead of hair fibres is necessary for the application of NR, to harness its unique capacity to resolve at a subnanometric level the layers formed by selected species, giving information on the chemical composition and hierarchy of adsorption.

Here, different types of hair-mimetic surfaces have been produced, increasing the accuracy of the models by using custom synthesised long-chain thiols.

These long-chain thiols showed a more complex behaviour than their short-chain counterparts and allowed the production of more specific (mixed) hair models, to more closely represent both healthy (18-MET/HDT mixture) and damaged (PS/18-MEA thiol) hair surfaces.

The first conclusion can be drawn regarding the chosen functionalization protocol: from the NR data of the thiol surfaces in pure solvent, it emerged that both the short-chain partially damaged (MBT/PS) and the mixed healthy hair models are adsorbed on the surface at a ratio corresponding to their proportion in solution, despite some differences in the structures. Instead, the deposition of the 18-MEA thiol on the gold surface is significantly more favoured than that of PS, requiring the latter to be in excess in solution (compared to the desired surface ratio). Nonetheless, the study proved the feasibility of producing and using such models of increased biomimetic character to gain a more detailed understanding of the adsorption properties of hair.

Two overarching conclusions were obtained. The first is the unexpected adsorption of the anionic surfactant SDS to the negatively charged surface representing a damaged hair fibre. This was observed not only on the pure sulphonate surface (the most surprising) but also on the partially damaged hair model containing 18-MEA, due to the formation of patches of different hydrophobicity. It has been confirmed by multiple experiments, and explained by the combination of two factors, i.e., the presence of a charge neutralizing layer of sodium ion on the sulphonate moieties and a preferential partitioning of dodecanol on the surface due to the penalty for the adsorption of the surfactant. Both factors were introduced to mimic a detergency scenario, so the result is of cosmetic relevance. No such behaviour was displayed by the short-chain mimetic of a partially damaged fibre, suggesting that this system might represent poorly the hair surface.

The second major result of the adsorption study concerns the use of chitosan as a more sustainable alternative to synthetic polymers. Taken together, the experiments have clearly proven that the methyl branch of 18-MEA has a major role in the adsorption of the polysaccharide. In fact, the presence of the oligomeric form of chitosan was not detected on surfaces formed by unbranched long-chain thiols, while it was visible on both pure 18-MET and on the more biomimetic 18-MET/HDT layer. There was a hint of such behaviour on the corresponding short-chain models (MBT and BT – on the former chitosan was irreversibly adsorbed while on the latter it was washed away in the final rinse), but their properties were not as remarkably different as on the long-chain model surfaces.

As pointed out earlier, the experiments have been designed to resemble as much as possible real conditions, using simplified solutions and isolating features of the hair surface, but mimicking factors that could influence the interaction (such as the salinity of the solution or the use of unpurified surfactants). The use of biomimetic surfaces is known in the literature, but the validity of their application to obtain cosmetically relevant results had not been previously investigated so deeply. Further studies will be required, however, to clarify some results presented in this thesis.

6 Points of perspective

This thesis has proven the feasibility and usefulness of using neutron reflectometry to investigate hair-mimetic models for cosmetic applications. However, the study is not complete, and several points may benefit from additional experiments.

The first example that may need clarification is the interaction of the partially damaged hair model with the natural and the synthetic polyelectrolytes presented in chapter 4 (and better detailed in paper III). The NR results seem to suggest a stronger interaction with chitosan than with pDADMAC, a desirable result which was not however proven unambiguously here. To do this, different scattering contrasts need to be used. The effect of the order of injection may also be examined, as it was shown to influence the structure of the adsorbed layers. If the adsorption of chitosan is confirmed to be more favourable than that of pDADMAC, additional studies could address how the molecular weight of chitosan influences this behaviour.

Moreover, the adsorption of these polymers may be further investigated using the more biomimetic mixed model, which was easily produced and showed interesting features.

The preferential partitioning of dodecanol on damaged hair models also needs further studies. The implication of the observed effect is that this mechanism could be used for the delivery of small, neutral molecules from anionic surfactant systems, selectively targeting the damaged regions of the hair fibre. The effect of different cations (e.g., potassium instead of sodium) or salt concentration could be addressed, as well as the effect of the hydrophobic chain length, to optimize delivery conditions.

In addition to the compounds studied here, other species could be selected, e.g., biosurfactants, to compare their action to that of the traditional surfactants that have been reported here.

The developed approach is versatile and could be adapted to answer similar questions on related systems, adding more specific information on the adsorption hierarchy that cannot be obtained by other surface techniques.

7 References

1. Tukker, A., Cohen, M. J., Hubacek, K. & Mont, O. Sustainable Consumption and Production. J of Industrial Ecology 14, 1–3 (2010).

2. Mont, O. & Plepys, A. Sustainable consumption progress: should we be proud or alarmed? Journal of Cleaner Production 16, 531–537 (2008).

3. Liobikienė, G. & Dagiliūtė, R. The relationship between economic and carbon footprint changes in EU: The achievements of the EU sustainable consumption and production policy implementation. Environmental Science & Policy 61, 204–211 (2016).

4. Cosmetics industry - statistics & facts | Statista. https://www.statista.com/topics/3137/cosmetics-industry/#topicOverview.

5. Luengo, G. S., Leonforte, F., Greaves, A., Rubio, R. G. & Guzman, E. Physico-chemical challenges on the self-assembly of natural and bio-based ingredients on hair surfaces: towards sustainable haircare formulations. Green Chemistry (2023).

6. Philippe, M., Didillon, B. & Gilbert, L. Industrial commitment to green and sustainable chemistry: using renewable materials & developing eco-friendly processes and ingredients in cosmetics. (2012).

7. Cornwell, P. A. A review of shampoo surfactant technology: consumer benefits, raw materials and recent developments. International Journal of Cosmetic Science (2017).

8. InnovaXN. https://www.innovaxn.eu/.

9. United Nations Sustainable Development. The content of this publication has not been approved by the United Nations and does not reflect the views of the United Nations or its officials or Member States. https://www.un.org/sustainabledevelopment/.

10. Cubas, A. L. V., Bianchet, R. T., Reis, I. M. A. S. D. & Gouveia, I. C. Plastics and Microplastic in the Cosmetic Industry: Aggregating Sustainable Actions Aimed at Alignment and Interaction with UN Sustainable Development Goals. Polymers 14, 4576 (2022).

11. L'Haridon, J., Martz, P., Chenéble, J. -C., Campion, J. -F. & Colombe, L. Ecodesign of cosmetic formulae: methodology and application. Intern J of Cosmetic Sci 40, 165–177 (2018).

12. Aranaz, I. et al. Chitosan: An Overview of Its Properties and Applications. (2021).

13. Guzmán, E., Ortega, F. & Rubio, R. G. Chitosan: A Promising Multifunctional Cosmetic Ingredient for Skin and Hair Care. Cosmetics 9, 99 (2022).

14. Hausman, L. A. Recent Studies of Hair Structure Relationships. The Scientific Monthly 30, 258–277 (1930).

15. Hashimoto, K. The structure of human hair. Clinics in Dermatology 6, 7–21 (1988).

16. Robbins, C. R. Morphological, Macromolecular Structure and Hair Growth. in Chemical and Physical Behavior of Human Hair 1–104 (Springer Berlin Heidelberg, Berlin, Heidelberg, 2012). doi:10.1007/978-3-642-25611-0_1.

17. Stanić, V., Bettini, J., Montoro, F. E., Stein, A. & Evans-Lutterodt, K. Local structure of human hair spatially resolved by sub-micron X-ray beam. Sci Rep 5, 17347 (2015).

18. Bertrand, L., Doucet, J., Simionovici, A., Tsoucaris, G. & Walter, P. Lead-revealed lipid organization in human hair. Biochimica et Biophysica Acta (BBA) - General Subjects 1620, 218–224 (2003).

19. Wilk, K. E., James, V. J. & Amemiya, Y. The intermediate filament structure of human hair. Biochimica et Biophysica Acta (BBA) - General Subjects 1245, 392–396 (1995).

20. Kreplak, L., Mérigoux, C., Briki, F., Flot, D. & Doucet, J. Investigation of human hair cuticle structure by microdiffraction: direct observation of cell membrane complex swelling. Biochimica et Biophysica Acta (BBA) - Protein Structure and Molecular Enzymology 1547, 268–274 (2001).

21. Birbeck, M. S. C. & Mercer, E. H. THE ELECTRON MICROSCOPY OF THE HUMAN HAIR FOLLICLE. The Journal of Cell Biology 3, 203–214 (1957).

22. Lindelöf, B. Human Hair Form: Morphology Revealed by Light and Scanning Electron Microscopy and Computer Aided Three-Dimensional Reconstruction. Arch Dermatol 124, 1359 (1988).

23. De Cássia Comis Wagner, R., Kiyohara, P. K., Silveira, M. & Joekes, I. Electron microscopic observations of human hair medulla. Journal of Microscopy 226, 54–63 (2007).

24. Hair Follicle. (Springer-Verlag, Tokyo, 2005). doi:10.1007/b138721.

25. Luengo, G. S., Fameau, A.-L., Léonforte, F. & Greaves, A. J. Surface science of cosmetic substrates, cleansing actives and formulations. Advances in Colloid and Interface Science 290, 102383 (2021).

26. Peet, D. J., Wettenhall, R. E. H., Rivett, D. E. & Allen, A. K. A comparative study of covalently-bound fatty acids in keratinized tissues. Comparative Biochemistry and Physiology Part B: Comparative Biochemistry 102, 363–366 (1992).

27. Wertz, P. W. & Downing, D. T. Integral lipids of human hair. Lipids 23, 878–881 (1988).

28. Coderch, L., Alonso, C., García, M. T., Pérez, L. & Martí, M. Hair Lipid Structure: Effect of Surfactants. Cosmetics 10, 107 (2023).

29. Mizuno, H., Luengo, G. S. & Rutland, M. W. Interactions between Crossed Hair Fibers at the Nanoscale. (2010).

30. Jones, L. N. & Rivett, D. E. The role of 18-methyleicosanoic acid in the structure and formation of mammalian hair fibres. Micron 28, 469–485 (1997).

31. Masukawa, Y., Tsujimura, H. & Imokawa, G. A systematic method for the sensitive and specific determination of hair lipids in combination with chromatography. Journal of Chromatography B 823, 131–142 (2005).

32. Bergendal, E. & Rutland, M. W. Unveiling Texture and Topography of Fatty Acid Langmuir Films: Domain Stability and Isotherm Analysis. Langmuir 40, 10468–10476 (2024).

33. Bergendal, E. et al. Tuneable interfacial surfactant aggregates mimic lyotropic phases and facilitate large scale nanopatterning. Nanoscale 13, 371–379 (2021).

34. Smith, J. R. & Swift, J. A. Maple syrup urine disease hair reveals the importance of 18-methyleicosanoic acid in cuticular delamination. Micron 36, 261–266 (2005).

35. Csuka, D. A., Csuka, E. A., Juhász, M. L. W., Sharma, A. N. & Mesinkovska, N. A. A systematic review on the lipid composition of human hair. Int J Dermatology 62, 404–415 (2023).

36. Kreplak, L. et al. Profiling lipids across Caucasian and Afro-American hair transverse cuts, using synchrotron infrared microspectrometry. Intern J of Cosmetic Sci 23, 369–374 (2001).

37. Thibaut, S. et al. Chronological ageing of human hair keratin fibres. Intern J of Cosmetic Sci 32, 422–434 (2010).

38. Tokunaga, S., Tanamachi, H. & Ishikawa, K. Degradation of Hair Surface: Importance of 18-MEA and Epicuticle. (2019).

39. Korte, M., Akari, S., Ku, H. & Luengo, G. S. Distribution and Localization of Hydrophobic and Ionic Chemical Groups at the Surface of Bleached Human Hair Fibers. (2014).

40. Llamas, S. et al. Adsorption of polyelectrolytes and polyelectrolytes-surfactant mixtures at surfaces: a physico-chemical approach to a cosmetic challenge. Advances in Colloid and Interface Science 222, 461–487 (2015).

41. Gonçalves, R. A., Holmberg, K. & Lindman, B. Cationic surfactants: A review. Journal of Molecular Liquids 375, 121335 (2023).

42. Holmberg, K., Jönsson, B., Kronberg, B. & Lindman, B. Surfactants and Polymers in Aqueous Solution. (Wiley, 2002). doi:10.1002/0470856424.

43. Zhou, W. The determination of 1,4-dioxane in cosmetic products by gas chromatography with tandem mass spectrometry. Journal of Chromatography A 1607, 460400 (2019).

44. Correia, E. L., Brown, N., Ervin, A., Papavassiliou, D. V. & Razavi, S. Contamination in Sodium Dodecyl Sulfate Solutions: Insights from the Measurements of Surface Tension and Surface Rheology. Langmuir 38, 7179–7189 (2022).

45. Jimoh, A. A. & Lin, J. Biosurfactant: A new frontier for greener technology and environmental sustainability. Ecotoxicology and Environmental Safety 184, 109607 (2019).

46. Akiyama, Y., Matsue, Y., Kasagawa, A., Mori, T. & Nishijima, S. Adsorption Behavior of Coacervates on the Human Hair Surface. Chemistry Letters 41, 1351–1353 (2012).

47. Del Giudice, A. et al. Towards natural care products: Structural and deposition studies of bio-based polymer and surfactant mixtures. Colloids and Surfaces A: Physicochemical and Engineering Aspects 698, 134365 (2024).

48. Sarkar, S. D., Farrugia, B. L., Dargaville, T. R. & Dhara, S. Chitosan–collagen scaffolds with nano/microfibrous architecture for skin tissue engineering. J Biomedical Materials Res 101, 3482–3492 (2013).

49. Tsai, S. et al. Preparation and cell compatibility evaluation of chitosan/collagen composite scaffolds using amino acids as crosslinking bridges. J of Applied Polymer Sci 105, 1774–1785 (2007).

50. Shukla, S. K., Mishra, A. K., Arotiba, O. A. & Mamba, B. B. Chitosan-based nanomaterials: A state-of-the-art review. International Journal of Biological Macromolecules 59, 46–58 (2013).

51. Lord, M. S. et al. Synthesis and characterization of water soluble biomimetic chitosans for bone and cartilage tissue regeneration. J. Mater. Chem. B 2, 6517–6526 (2014).

52. Chiappisi, L. & Gradzielski, M. Co-assembly in chitosan–surfactant mixtures: thermodynamics, structures, interfacial properties and applications. Advances in Colloid and Interface Science (2015).

53. Schober, H. An introduction to the theory of nuclear neutron scattering in condensed matter. Journal of Neutron Research 17, 109–357 (2014).

54. Neutron Activation and Scattering Calculator. https://www.ncnr.nist.gov/resources/activation/.

55. McCluskey, A. R. Neutron reflectometry analysis: using model-dependent methods. Preprint at https://doi.org/10.48550/ARXIV.2003.08270 (2020).

56. Wolff, M. & Gutfreund, P. Neutron reflectivity for the investigation of coatings and functional layers. in Handbook of Modern Coating Technologies 143–175 (Elsevier, 2021). doi:10.1016/B978-0-444-63239-5.00004-4.

57. Kiessig, H. Interferenz von Röntgenstrahlen an dünnen Schichten. Annalen der Physik 402, 769–788 (1931).

58. Parratt, L. G. Surface Studies of Solids by Total Reflection of X-Rays. Phys. Rev. 95, 359–369 (1954).

59. Abelès, F. Sur la propagation des ondes électromagnétiques dans les milieux sratifiés. Ann. Phys. 12, 504–520 (1948).

60. Majkrzak, C. F. & Berk, N. F. Exact determination of the phase in neutron reflectometry. Phys. Rev. B 52, 10827–10830 (1995).

61. Zhou, X.-L. & Chen, S.-H. Theoretical foundation of X-ray and neutron reflectometry. Physics Reports 257, 223–348 (1995).

62. Heavens, O. S. Optical properties of thin films. Rep. Prog. Phys. 23, 1–65 (1960).

63. Cousin, F. & Fadda, G. An introduction to neutron reflectometry. EPJ Web Conf. 236, 04001 (2020).

64. Fragneto-Cusani, G. Neutron reflectivity at the solid/liquid interface: examples of applications in biophysics.

65. Neutron Data Booklet. (Old City, Philadelphia, PA, 2003).

66. Sauerbrey, G. Verwendung von Schwingquarzen zur Wägung dünner Schichten und zur Mikrowägung. Z. Physik 155, 206–222 (1959).

67. Reviakine, I., Johannsmann, D. & Richter, R. P. Hearing What You Cannot See and Visualizing What You Hear: Interpreting Quartz Crystal Microbalance Data from Solvated Interfaces. Anal. Chem. 83, 8838–8848 (2011).

68. Voinova, M. V., Rodahl, M., Jonson, M. & Kasemo, B. Viscoelastic Acoustic Response of Layered Polymer Films at Fluid-Solid Interfaces: Continuum Mechanics Approach. Phys. Scr. 59, 391–396 (1999).

69. Balzer, D., Varwig, S. & Weihrauch, M. Viscoelasticity of personal care products. Colloids and Surfaces A: Physicochemical and Engineering Aspects 99, 233–246 (1995).

70. Tiraferri, A., Maroni, P. & Rodr, D. C. Mechanism of Chitosan Adsorption on Silica from Aqueous Solutions. (2014).

71. Dhopatkar, N., Park, J. H., Chari, K. & Dhinojwala, A. Adsorption and Viscoelastic Analysis of Polyelectrolyte–Surfactant Complexes on Charged Hydrophilic Surfaces. (2015).

72. Binnig, G., Quate, C. F. & Gerber, Ch. Atomic Force Microscope. Phys. Rev. Lett. 56, 930–933 (1986).

73. Dzedzickis, A., Rožėnė, J., Bučinskas, V., Viržonis, D. & Morkvėnaitė-Vilkončienė, I. Characteristics and Functionality of Cantilevers and Scanners in Atomic Force Microscopy. Materials 16, 6379 (2023).

74. Moreno-Herrero, F., Colchero, J., Gómez-Herrero, J. & Baró, A. M. Atomic force microscopy contact, tapping, and jumping modes for imaging biological samples in liquids. Phys. Rev. E 69, 031915 (2004).

75. García, R. & San Paulo, A. Attractive and repulsive tip-sample interaction regimes in tapping-mode atomic force microscopy. Phys. Rev. B 60, 4961–4967 (1999).

76. Dokukin, M. E. & Sokolov, I. Quantitative Mapping of the Elastic Modulus of Soft Materials with HarmoniX and PeakForce QNM AFM Modes. Langmuir 28, 16060–16071 (2012).

77. Alessandrini, A. & Facci, P. AFM: a versatile tool in biophysics. Meas. Sci. Technol. 16, R65–R92 (2005).

78. Love, J. C., Estroff, L. A., Kriebel, J. K., Nuzzo, R. G. & Whitesides, G. M. Self-Assembled Monolayers of Thiolates on Metals as a Form of Nanotechnology.

79. Gooding, J. J., Mearns, F., Yang, W. & Liu, J. Self-Assembled Monolayers into the 21st Century: Recent Advances and Applications. (2003).

80. Besharat, Z. et al. Mixed monolayers of alkane thiols with polar terminal group on gold: Investigation of structure dependent surface properties. Journal of Colloid and Interface Science 484, 279–290 (2016).

81. Guzmán, E. et al. Adsorption of Conditioning Polymers on Solid Substrates with Different Charge Density. ACS Appl. Mater. Interfaces 3, 3181–3188 (2011).

82. Guzmán, E., Ortega, F., Baghdadli, N., Luengo, G. S. & Rubio, R. G. Effect of the molecular structure on the adsorption of conditioning polyelectrolytes on solid substrates. Colloids and Surfaces A: Physicochemical and Engineering Aspects 375, 209–218 (2011).

83. Guzmán, E. et al. Effect of a natural amphoteric surfactant in the bulk and adsorption behavior of polyelectrolyte-surfactant mixtures. Colloids and Surfaces A: Physicochemical and Engineering Aspects 585, 124178 (2020).

84. Vericat, C. et al. Surface characterization of sulfur and alkanethiol self-assembled monolayers on Au(111).

85. ChemDraw | Revvity Signals Software. https://revvitysignals.com/products/research/chemdraw.

86. National Deuteration Facility | Research Facilities | ANSTO. https://www.ansto.gov.au/facilities/national-deuteration-facility.

87. Mokrani, C., Fatisson, J., Guérente, L. & Labbé, P. Structural Characterization of (3-Mercaptopropyl)sulfonate Monolayer on Gold Surfaces. Langmuir 21, 4400–4409 (2005).

88. Mukerjee, P. Critical micelle concentrations of aqueous surfactant systems.

89. Zhang, C. et al. Impact of NaCl concentration on equilibrium and dynamic surface adsorption of cationic surfactants in aqueous solution. Journal of Molecular Liquids 238, 423–429 (2017).

90. Beyer, K., Leine, D. & Blume, A. The demicellization of alkyltrimethylammonium bromides in 0.1M sodium chloride solution studied by isothermal titration calorimetry. Colloids and Surfaces B: Biointerfaces 49, 31–39 (2006).

91. Devishvili, A. et al. SuperADAM: Upgraded polarized neutron reflectometer at the Institut Laue-Langevin. Review of Scientific Instruments 84, 025112 (2013).

92. Campbell, R. A., Wacklin, H. P., Sutton, I., Cubitt, R. & Fragneto, G. FIGARO: The new horizontal neutron reflectometer at the ILL. Eur. Phys. J. Plus 126, 107 (2011).

93. Saerbeck, T. et al. Recent upgrades of the neutron reflectometer D17 at ILL. J Appl Crystallogr 51, 249–256 (2018).

94. Webster, J., Holt, S. & Dalgliesh, R. INTER the chemical interfaces reflectometer on target station 2 at ISIS. Physica B: Condensed Matter 385–386, 1164–1166 (2006).

95. James, M., Nelson, A., Brule, A. & Schulz, J. C. Platypus: a time-of-flight neutron reflectometer at Australia's new research reactor. Journal of Neutron Research 14, 91–108 (2006).

96. Pilkington, G. A. et al. Electro-responsivity of ionic liquid boundary layers in a polar solvent revealed by neutron reflectance. The Journal of Chemical Physics 148, 193806 (2018).

97. Amann-Winkel, K. et al. X-ray and Neutron Scattering of Water. Chem. Rev. 116, 7570–7589 (2016).

98. GitHub - Alexey-Klechikov/pySAred: SuperADAM hdf5 files reduction software. https://github.com/Alexey-Klechikov/pySAred.

99. Gutfreund, P. et al. Towards generalized data reduction on a chopper-based time-of-flight neutron reflectometer. J Appl Crystallogr 51, 606–615 (2018).

100. Arnold, O. et al. Mantid—Data analysis and visualization package for neutron scattering and μ SR experiments. Nuclear Instruments and Methods in Physics Research Section A: Accelerators, Spectrometers, Detectors and Associated Equipment 764, 156–166 (2014).

101. Nelson, A. R. J. & Prescott, S. W. refnx : neutron and X-ray reflectometry analysis in Python. J Appl Crystallogr 52, 193–200 (2019).

102. Roughness and microslicing — A Guide to Reflectometry. https://www.reflectometry.org/learn/3_reflectometry_slab_models/roughness_and_microslicing.html#microslicing.

103. Wormington, M., Panaccione, C., Matney, K. M. & Bowen, D. K. Characterization of structures from X-ray scattering data using genetic algorithms. Philosophical Transactions of the Royal Society of London. Series A: Mathematical, Physical and Engineering Sciences 357, 2827–2848 (1999).

104. Garreau, C. et al. Preparation of highly stable and ultrasmooth chemically grafted thin films of chitosan. Soft Matter 19, 1606–1616 (2023).

105. Mazzer, A. R. et al. Neutron reflectivity measurement of protein A–antibody complex at the solid-liquid interface. Journal of Chromatography A 1499, 118–131 (2017).

106. Campbell, R. A. Recent advances in resolving kinetic and dynamic processes at the air/water interface using specular neutron reflectometry. Current Opinion in Colloid & Interface Science 37, 49–60 (2018).

107. Philippoff, W. Relaxations in Polymer Solutions, Liquids, and Gels. in Physical Acoustics vol. 2 1–90 (Elsevier, 1965).

108. Gwyddion – Free SPM (AFM, SNOM/NSOM, STM, MFM, …) data analysis software. http://gwyddion.net/.

109. Cossaro, A. et al. X-ray Diffraction and Computation Yield the Structure of Alkanethiols on Gold(111). Science 321, 943–946 (2008).

110. Camillone, N., Chidsey, C. E. D., Liu, G. & Scoles, G. Superlattice structure at the surface of a monolayer of octadecanethiol self-assembled on Au(111). The Journal of Chemical Physics 98, 3503–3511 (1993).

111. Liu, G. et al. An unexpected packing of fluorinated n -alkane thiols on Au(111): A combined atomic force microscopy and x-ray diffraction study. The Journal of Chemical Physics 101, 4301–4306 (1994).

112. Li, N., Thomas, R. K. & Rennie, A. R. Effect of pH, surface charge and counter-ions on the adsorption of sodium dodecyl sulfate to the sapphire/solution interface. Journal of Colloid and Interface Science 378, 152–158 (2012).

113. Wang, Q. et al. Atomistic Characterization of Healthy and Damaged Hair Surfaces: A Molecular Dynamics Simulation Study of Fatty Acids on Protein Layer. ChemBioChem 25, e202400128 (2024).

114. Hlawacek, G., Ahmad, I., Smithers, M. A. & Kooij, E. S. To see or not to see: Imaging surfactant coated nano-particles using HIM and SEM. Ultramicroscopy 135, 89–94 (2013).

115. Carambassis, A., Jonker, L. C., Attard, P. & Rutland, M. W. Forces Measured between Hydrophobic Surfaces due to a Submicroscopic Bridging Bubble. Phys. Rev. Lett. 80, 5357–5360 (1998).

116. Zhang, X. H., Quinn, A. & Ducker, W. A. Nanobubbles at the Interface between Water and a Hydrophobic Solid. Langmuir 24, 4756–4764 (2008).

117. Schwendel, D. et al. Interaction of Water with Self-Assembled Monolayers: Neutron Reflectivity Measurements of the Water Density in the Interface Region. Langmuir 19, 2284–2293 (2003).

118. Hernández-Rivas, M. et al. Deposition of Synthetic and Bio-Based Polycations onto Negatively Charged Solid Surfaces: Effect of the Polymer Cationicity, Ionic Strength, and the Addition of an Anionic Surfactant. Colloids and Interfaces 4, 33 (2020).